Journal of Molecular Structure 1246 (2021) 131203

Contents lists available at ScienceDirect

Journal of Molecular Structure

journal homepage: www.elsevier.com/locate/molstr

Synthesis and characterization of new metal complexes containing Triazino[5,6–b]indole moiety: *In vitro* DNA and HSA binding studies

Reem L.B. Alanazi, Mehvash Zaki*, Wafa A. Bawazir

Department of Chemistry, King Abdulaziz University, P.O. Box 80203, Jeddah, Saudi Arabia

ARTICLE INFO

Article history:
Received 18 March 2021
Revised 24 July 2021
Accepted 27 July 2021
Available online 28 July 2021

Keywords:
Triazino[5,6–b]indole
Cu(II)/Ni(II) metal complexes
In vitro DNA binding
HSA binding
FRET
Molecular docking

ABSTRACT

The present study reports the synthesis, structural characterization of Ni(II) (**1,3**) and Cu(II) (**2,4**) metal complexes of Schiff-base (**L**) derived from 5H-[1,2,4]triazino[5,6-b]indol-3-amine and salicylaldehyde moiety. The coordination sphere of Cu(II)/Ni(II) was completed by tethering secondary ligand 2,2′–Bipyridine and 1,10 phenanthroline to obtain the final complexes **1**–**4**, respectively. The spectral analysis of complexes **1** and **3** suggested square planar geometry while complexes **2** and **4** acquire the octahedral geometry around the metal centers. *In vitro* DNA binding profiles of the newly synthesized metal complexes **1**–**4** with calf thymus DNA (CT DNA) were explored by employing electronic absorption titrations and fluorescence spectral studies. The results revealed that complexes **1**–**4** bind to DNA through electrostatic surface binding mode along with partial intercalation in the minor groove. Moreover, complexes **3** and **4** have stronger DNA binding propensity with higher intrinsic binding constant K_b values of 1.9×10^4 and 4.8×10^4 M^{-1}, respectively. Additionally, HSA binding studies of ligand **L** and metal complexes **1**–**4** support the static quenching mechanism and alterations in the microenvironment around Trp–214 residues causing conformational distortions in the HSA secondary structure. Furthermore, molecular docking studies of complexes **3** and **4** with DNA and HSA confirms that both specifically binds in G–C rich regions of the DNA minor groove and subdomain IIA pocket of HSA near the Trp–214 residue.

1. Introduction

The interaction of metal complexes with DNA is one of the most emerging areas of inorganic medicinal chemistry. In the recent years, rapid advances has been made for the development of the new improved metal based drugs whose ultimate target is DNA [1–3]. The design of an organic framework that enhances the DNA binding ability of metal complexes is necessary in order to overcome the drawbacks related to platinum drugs. The literature revealed that many DNA binding agents that bind with DNA through non–covalent interactions such as groove binding, intercalation and electrostatic interaction is crucial for the development of chemotherapeutic drugs [4–6]. Therefore, an approach to improve the DNA binding potential of metal complexes is the use of planar aromatic pharmacophore containing heteroatom's that provides the coordinating center for the metal ion in order to structurally feature the molecule for the better stacking interaction within the base pairs of the DNA helix. This brings about conformational changes in DNA. In this regard, 1,2,4 triazine moieties are considered as the attractive heterocyclic scaffold owing to its resemblance with purines and broad biological properties such as anti-inflammatory, antimicrobial and antitumor activity [7–9]. The combination of 1,2,4 triazine moieties with other heterocyclic structures such as indole, pyrazole and thiophene rings leads to the generation of ligand scaffold with enhanced pharmacological properties [10]. This synthesized triazino[5,6*b*]indole amine and its derivatives exhibited a wide range of biological activities such as antiparasitic, antihypertensive, antimalarial, antibacterial, and antifungal activities [11–15]. *In vitro* studies of triazino[5,6*b*] indoles had shown that most of them act as antiviral agents specifically against rhinovirus [16]. Moreover, the formation of Schiff base molecule by the condensation of bioactive triazino[5,6*b*]indole amine with salicylaldehyde leads to the development of new chemotherapeutic agents. Furthermore, tethering the biologically active Schiff base ligand with transition metal ions increases the pharmacological activity manyfold, facilitates the DNA interaction and improves the therapeutic potential [17]. In the past decade, the interaction of many Schiff base transition metal complexes with DNA has been investigated because DNA is easily prone to damage thereby inducing the cellular degradation in diseased cells [18]. In particular, Schiff base Cu(II) and Ni(II) metal complexes exhibited interesting biological properties (such as antipyretic, anti-inflammatory, anti-diabetic, anti-bacterial, anti-HIV

* Corresponding author.
E-mail address: mehvashzaki@gmail.com (M. Zaki).

https://doi.org/10.1016/j.molstruc.2021.131203
0022-2860/

and anti-cancer), structural versatility and the ability to mimic metallo-enzymes used in the catalytic oxidation/reduction in biological reactions [19–21].

Apart from this, the selectivity of complexes can be further increased by using some carrier molecules that can safely deliver the complexes inside the tumor cells. The human serum albumin (HSA), which is abundantly available biomacromolecular carrier present in our circulatory system helps in the biodistribution of various exogenous and endogenous molecules. These molecules includes vitamins, hormones, metabolites, fatty acids, and drug molecules. Furthermore, HSA also contribute in the transportation of metal ions like Cu^{2+} and $Ni^{2+}$to regulate the osmotic pressure of blood [22,23]. The HSA acts as biomacromolecular carrier by binding to the molecules in its binding site. In general, HSA has two binding sites present inside its structure called Sudlow's site I and Sudlow's site II present in hydrophobic cavities in subdomain IIA and IIIA, respectively. But in some cases molecule also prefers a third binding site III located in the hydrophobic pocket of subdomain IB [24]. Therefore, the binding interaction of metal complexes with HSA is extremely important in the path of the drug development process as it is well known that HSA selectively accumulates inside the tumor cells leaving the healthy cells thereby reducing the toxicity caused by the drug in the human body [25].

Herein, we describe the synthesis, characterization of new Cu(II)/Ni(II) transition metal complexes [Ni(L)(Bipy)]1/2SO_4(**1**), [Cu(L)(Bipy)]1/2SO_4(**2**), [Ni(L)(Phen)]1/2SO_4(**3**) and [Cu(L)(Phen)]1/2SO_4(**4**)derived from new ligand (E)–2–(((5H–[1,2,4]triazino[5,6–b]indol–3–yl)imino)methyl)phenol(**L**). This new Schiff base ligand scaffold is not reported in the literature and thus requires extensive investigation in the field of medicinal chemistry. The newly designed pharmacophoric ligand framework was mainly achieved by the reaction of isatin and aminoguanidine which further reacted with salicylaldehyde to produce ligand **L**. In this regard, a comparative *in vitro* DNA binding pattern of ligand **L** and complexes **1**–**4** was thoroughly studied by employing biophysical studies. Furthermore, in order to get insight into the delivery process by serum protein HSA, the *in vitro* HSA of ligand **L** and metal complexes **1**–**4**were conducted under physiological conditions. Finally, the molecular docking studies of complex **4** showing stronger binding affinity with DNA and HSA were performed to determine the specific interaction of complex within the binding site of biomacromolecules.

2. Experimental section

2.1. Reagents and materials

All reagents were commercially purchased and used as provided without extra purification. Nickel sulfate hexahydrate, Copper sulfate hexahydrate salicylaldehyde (Sigma–Aldrich), Isatin (Sigma–Aldrich), Aminoguanidine (Sigma–Aldrich), 1,10 Phenanthroline, 2,2′–Bipyridine (Sigma–Aldrich) and disodium salt of calf thymus DNA (purely polymerized stored at 4°C). Trisaminomethane (TRIS) buffer was also handled as received from Sigma–Aldrich. The solvents were purchased from Merck in high purity. All reagents were of the optimal financial grade and were used without any additional purification.

2.2. Methods and instrumentation

Carbon, hydrogen, and nitrogen percentage were resolved using the CHNSO Elemental Analyzer Elementar Vario EL III model. Molar conductance was calculated using CON 510 Bench conductivity TDS Meter at room temperature. The melting point of compounds has been measured on the Sanyo GallenKamp melting point apparatus. The ^{1}H and ^{13}C NMR spectra have been recorded on Bruker 600 Ultrashield NMR 600/S4/MKS spectrometer. IR spectrum was measured on Interspec 2020 FTIR spectrometer in KBr pellets from 400–4000 cm^{-1}. Electrospray mass spectra were conducted on the Micromass Quattro II mass spectrometer. The electronic spectrum was taken on Shimadzu MultiSpec–1501 UV–vis spectrophotometer in DMF using 1 cm path length cuvettes. The information was recorded in λ_{max}/nm. Fluorescence measurements were resolute on Hitachi (F–7000) fluorescence spectrophotometers. A complete set of experiments dealing with the interaction of ligand and complexes with CT–DNA was accomplished in buffer (5 mM Tris–HCl, 50 mM NaCl, pH = 7.3).

2.3. Synthesis

2.3.1. Synthesis of the ligand (*L*)

The solution of isatin (1.47 g, 10 mmol) dissolved in ethanol was added to a solution of aminoguanidine (1.10 g, 10 mmol) also dissolved in 10 ml methanol and the resulting mixture was refluxed continuously for 5 h to obtain the required ligand in good yield. The molecule obtained was isolated and further reacted with salicylaldehyde (1.22 g, 10 mmol) until the dark yellow color precipitate of ligand **L** was obtained in the required amount. The dark yellow color precipitate was carefully filtered by Buchner and washed several times with methanol and hexane, dried in a desiccator.

Yield = 92%, M.P. 285 °C. Anal. (%) Calc. for $C_{16}H_{11}N_5O$: C, 66.43; H, 3.83; N, 24.21. Found: C, 66.35; H, 3.41; N, 24.27. IR (KBr) (ν_{max} /cm^{-1}): 3430.69 υ(O–H)$_{stretch}$; 3197.98, 3067.66 υ(C–H)$_{stretch}$; 1157.91 υ(C–H)$_{bend}$ {in–plane aromatic}; 751.60 υ(C–H)$_{bend}$ {out–plane aromatic}; 1616.56 υ(C=N); 1537.86 υ(C=C); 1256.20 υ(C–O). ^{1}H NMR (400 MHz, DMSO–d_6, δ): 12.57 (–OH); 10.26 (–NH, indole); 8.91 (–CH=N); 6.53, 6.68, 7.0, 7.08, 7.11, 7.51, 7.67, 8.04 (aromatic–H, **L**); 3.4 (CH_3–DMSO). ^{13}C NMR (100 MHz, DMSO–d_6, δ): 164.8 (–CH=N); 109.9, 113.7, 115.5, 120.1, 125.9, 129.6, 133.6, 137.1, 143.8, 147.8, 153.4 (Ar C–triazine); 161.3, 116.1, 117.7, 122.95, 127.3, 131.4, 133.6, (Ar C–salicylaldehyde). Uv–vis (1×10^{-3} M, DMF, nm): 280 (π –π^*, strong), 320 (n–π^*, strong). ESI–MS (m/z, DMF) 290.3 $[C_{16}H_{11}N_5O + H^+]^+$ (Fig. S2).

2.3.2. Synthesis of the complex (*1*)

The solution of Triazino[5,6–b]indole ligand **L** (0.289 g, 1.0 mmol) was obtained in 5 ml of DMF after 10 min of heating. The metal salt $NiSO_4.6H_2O$ (0.31 g, 1.2 mmol) dissolved in a minimum amount of distilled water was added to the hot solution of ligand **L**. On the addition of metal salt, the color of the solution changes from orange to brown along with the appearance of some precipitate. The resulting solution was refluxed for 3 h and the 2,2′–Bipyridine (0.18 g, 1.2 mmol) dissolved in DMF was slowly added to the refluxing solution which causes a slight change in color along with the disappearance of the precipitate. The solution obtained was further refluxed for 4 h at 80 °C and finally, the solution was reduced and left for 7 days in the cupboard. After a week brown color crystalline product was obtained and this complex **1** was washed several times with a 1:1 methanol and dichloromethane solution and dried in vacuo.

Yield = 75%, M.P. 279 °C, Anal. (%) Calc. for $C_{26}H_{18}N_7NiO_5S_{0.5}$: C, 62.06; H, 3.61; N, 19.49. Found: C, 62.35; H, 3.41; N, 19.27. Λ_M (1×10^{-3} M, DMF): 110 Ω^{-1} cm^2 mol^{-1}. IR (KBr) (ν_{max} /cm^{-1}): 3078.14 υ(C–H) $_{stretch}$; 1099.08 υ(C–H)$_{bend}$ {in–plane aromatic}; 765.81 υ(C–H)$_{bend}$ {out–plane aromatic}; 1599.91 υ(C=N); 1564.77 υ(C=C); 1262.35 υ(C–O); 417.19 υ(Ni–N), 523.16 υ(Ni–O). ^{1}H NMR (400 MHz, DMSO–d_6, δ): 9.50 (–NH, indole); 8.98 (–CH=N); 7.90–6.70 (aromatic–H, **L** and phen); 3.44 (H_2O); 2.49 (CH_3–DMSO). ^{13}C NMR (100 MHz, DMSO–d_6, δ): 173.0 (–CH=N); 125.9, 129.6, 132.18, 134.2, 148.0, 156.9 (Ar C, Phenan); 110.7, 112.0, 115.5, 117.7, 118.8, 122.0, 127.5, 128.3, 131.8, 132.1, 134.9,

134.4, 140.3, 143.4, 147.5, 152.8, 160.4 (Ar C–ligand **L**); Uv–vis (1×10^{-3} M, DMF, nm): 275 (π –π^*), 325 (n–π^*), 480 (LMCT), 535 ($^1A_1g \rightarrow {}^1A_2g$), 620 ($^1A_1g \rightarrow {}^1B_1g$). ESI–MS (m/z, DMF) 552.03 $[C_{26}H_{18}N_7NiO_5S_{0.5} + H^+]^+$.

2.3.3. Synthesis of the complex (**2**)

Similarly, the solution of Triazino[5,6–b]indole ligand **L** (0.289 g, 1.0 mmol) was obtained in 5 ml of DMF after 10 min of heating. The $CuSO_4.6H_2O$ (0.32 g, 1.2 mmol) solution prepared in 3 ml of DMF, was gradually added to the hot solution of ligand **L** until a dark green color solution was obtained. The resulting solution was refluxed for 4 h and the 2,2′–Bipyridine (0.18 g, 1.2 mmol) dissolved in DMF was slowly added to the refluxing solutions which cause the appearance of the dark green color precipitate. The solution obtained was further refluxed for 2 h at 80 °C and the precipitate obtained was left overnight. The next day, the dark green color product was filtered and washed several times with a 1:1 methanol and dichloromethane solution and dried in vacuo.

Yield = 89%, M.P. 125 °C, Anal. (%) Calc. for $C_{26}H_{22}N_7CuO_5S_{0.5}$: C, 57.40; H, 4.08; N, 18.02. Found: C, 57.35; H, 4.02; N, 18.10. Λ_M (1×10^{-3} M, DMF): 112 Ω^{-1} cm^2 mol^{-1}. IR (KBr) (ν_{max} /cm^{-1}): 3429.81 υ(O–H)$_{stretch}$; 3050.21 υ(C–H) $_{stretch}$; 1123.67 υ(C–H)$_{bend}$ {in–plane aromatic}; 770.71 υ(C–H)$_{bend}$ {out–plane aromatic}; 1589.21 υ(C=N); 1603.08 υ(C=C); 1257.91 υ(C–O); 427.92 υ(Cu–N), 525.80 υ(Cu–O). Uv–vis (1×10^{-3} M, DMF, nm): 280 (π –π^*, strong), 300 (n–π^*, strong), 490 (LMCT), 600, 680 ($^2Eg \rightarrow {}^2T_2g$, broad). ESI–MS (m/z, DMF) 595.51 $[C_{26}H_{22}N_7CuO_5S_{0.5} + 3H^+]^+$.

2.3.4. Synthesis of the complex (**3**)

Similar to complex **1**, Triazino[5,6–b]indole ligand **L** (0.289 g, 1.0 mmol) was dissolved in 5 ml of DMF after 10 min of heating. The metal salt $NiSO_4.6H_2O$ (0.31 g, 1.2 mmol) dissolved in a minimum amount of distilled water was added to the hot solution of ligand **L**. On the addition of metal salt, the color of the solution changes from orange to brown along with the appearance of the precipitate. The resulting solution was refluxed for 3 h and the 1,10 phenanthroline (0.21 g, 1.2 mmol) dissolved in DMF was slowly added to the refluxing solution which causes the disappearance of the precipitate and the change in color from light brown to dark brown. The clear solution obtained was further refluxed for 4 h at 80 °C and was reduced and left for 7–8 days in the cupboard. After a week brown color product obtained was isolated and washed several times with a 1:1 methanol and dichloromethane solution and dried in vacuo.

Yield = 87%, M.P. >300 °C, Anal. (%) Calc. for $C_{28}H_{18}N_7NiO_3S_{0.5}$: C, 63.79; H, 3.44; N, 18.60. Found: C, 63.35; H, 3.41; N, 18.27. Λ_M (1×10^{-3} M, DMF): 120 Ω^{-1} cm^2 mol^{-1}. IR (KBr) (ν_{max} /cm^{-1}): 3054.01 υ(C–H) $_{stretch}$; 1122.67 υ(C–H)$_{bend}$ {in–plane aromatic}; 853.43 υ(C–H)$_{bend}$ {out–plane aromatic}; 1581.38 υ(C=N); 1607.51 υ(C=C); 1215.95 υ(C–O); 426.12 υ(Ni–N), 525.45 υ(Ni–O). ^{1}H NMR (400 MHz, DMSO–d_6, δ): 9.57 (–NH, indole); 8.99 (–CH=N); 7.94, 7.59, 7.39, 7.19, 6.95, 6.83 (aromatic–H, **L** and phen); 3.37 (H_2O); 2.49 (CH_3–DMSO). ^{13}C NMR (100 MHz, DMSO–d_6, δ): 173.55 (–CH=N); 126.2, 129.7, 132.7, 134.5, 148.4, 156.01 (Ar C, Phenan); 110.2, 112.0, 115.9, 117.7, 118.7, 122.2, 127.3, 128.4, 131.2, 132.7, 133.9, 134.4, 140.1, 143.2, 147.4, 151.3, 160.7 (Ar C–ligand **L**). Uv–vis (1×10^{-3} M, DMF, nm): 281 (π –π^*, strong), 319 (n–π^*, strong), 480 (LMCT) 550 ($^1A_1g \rightarrow {}^1A_2g$, broad), 625 ($^1A_1g \rightarrow {}^1B_1g$, broad). ESI–MS (m/z, DMF) 576.34 $[C_{28}H_{18}N_7NiO_3S_{0.5} + H^+]^+$.

2.3.5. Synthesis of the complex (**4**)

Similar to complex **2**, the solution of Triazino[5,6–b]indole ligand **L** (0.289 g, 1.0 mmol) was obtained in 5 ml of DMF after 10 min of heating in a round bottom flask. In the beaker $CuSO_4.6H_2O$ (0.32 g, 1.2 mmol) dissolved in 3 ml of DMF was gradually added to the hot solution of ligand **L** until a dark color solution was obtained. The resulting solution was refluxed for 4 h and after this, the 1,10 phenanthroline (0.21 g, 1.2 mmol) dissolved in DMF was added drop by drop to the refluxing solution leading to the formation of a dark green color precipitate. The solution obtained was further refluxed for 2.5 h at 80 °C and the precipitate obtained was left overnight. The next day the dark green color precipitate was filtered and washed several times with a 1:1 methanol and dichloromethane solution and dried in vacuo.

Yield = 90%, M.P. 195 °C, Anal. (%) Calc. for $C_{28}H_{22}N_7CuO_5S_{0.5}$: C, 59.20; H, 3.90; N, 17.26. Found: C, 59.35; H, 3.12; N, 17.50. Λ_M (1×10^{-3} M, DMF): 125 Ω^{-1} cm^2 mol^{-1}. IR (KBr) (ν_{max} /cm^{-1}): 3430.63 υ(O–H)$_{stretch}$; 3056.98 υ(C–H) $_{stretch}$; 1164.69 υ(C–H)$_{bend}$ {in–plane aromatic}; 856.77 υ(C–H)$_{bend}$ {out–plane aromatic}; 1593.42 υ(C=N); 1609.22 υ(C=C); 1220.63 υ(C–O); 420.31 υ(Cu–N), 520.13 υ(Cu–O). Uv–vis (1×10^{-3} M, DMF, nm): 285 (π –π^*, strong), 320 (n–π^*, strong), 492 (LMCT), 635, 695 ($^2Eg \rightarrow {}^2T_2g$, broad). ESI–MS (m/z, DMF) 617.43 $[C_{28}H_{22}N_7CuO_5S_{0.5} + H^+]^+$.

2.4. DNA binding evaluations

Absorption spectral study experiments were conducted by gradually adding increasing DNA concentration to a constant volume of complexes (50 μM) in each set. The intrinsic binding constant (K_b) were calculated from the changes in the variations in absorbance at the maximum wavelength of the intra ligand band and the K_b value was evaluated by using Wolf–Shimmer Eq. (1) [26];

$$\frac{[DNA]}{\varepsilon_a - \varepsilon_f} = \frac{[DNA]}{\varepsilon_b - \varepsilon_f} + \frac{1}{K_b(\varepsilon_a - \varepsilon_f)} \quad (1)$$

where, [DNA], ε_a, ε_f and ε_b are the amount of the DNA added, apparent extinction coefficient, extinction coefficient, apparent extinction coefficient for free complex and fully bound complex, respectively. However, the K_b values were calculated from the ratio of slope to intercept in the [DNA]/(ε_a–ε_f) vs [DNA] graph.

Steady state fluorescence emission studies in the range of 300–800 nm were also performed by employing a methodology identical to the electronic absorption titration studies and the binding propensity of complexes were evaluated using the Scatchard Eq. (2) and (3) [27];

$$C_f = C_T(I/I_o - P)(1 - P) \quad (2)$$

$$r/C_f = K(n - r) \quad (3)$$

where C_T is the total concentration of the complex, C_f is the concentration of free complex, added, I and I_o are fluorescence intensities in the presence and absence of CT–DNA, respectively, and P is the ratio of the observed fluorescence intensity of the bound complex to that of the free complex. The value of P was determined from the intercept by plotting the graph of I/I_o vs. 1/[DNA], r indicates the ratio of C_B (= C_T – C_f) to the concentration of DNA, where C_b represents the concentration of complex in the bounded DNA (r =C_b/[DNA]). The binding parameters K is the binding constant was calculated from the slope and "n" is the binding site number was determined from the intercept from the Plot of r/C_f *versus* r.

Similarly, in Ethidium bromide displacement studies, the EB–DNA solution was prepared by mixing 100 μM CT–DNA and 100 μM EB in an aqueous buffer incubated for 30 min before being used for titrations with metal complexes. The competitive interaction studies of complexes towards CT–DNA were evaluated by gradually adding the volume of interacting complexes to the solution of EB–DNA in each set where EB is almost fully bound to DNA helix. The impact of the EB–DNA solution on adding the increasing concentration of ligand/ metal complexes was directly impacted the change in the emission profile of EB–DNA [28]. For this

experiment Stern–Volmer equation was employed to calculate the Stern–Volmer quenching constant from the graph of F_o/F versus [Q]. In this Eq. (4), F_o and F is the fluorescence intensity in the absence and the presence of the complex, respectively and [Q] is the concentration of quencher i.e the ligand or metal complex.

$$\frac{F_o}{F} = 1 + K_{SV}[Q] \quad (4)$$

2.5. Molecular docking studies

The inflexible molecular docking studies were executed by using HEX 6.1 software [29]. Structures of the ligand/complexes were drawn using CHEMSKETCH (http://www.acdlabs.com) which was changed into PDB format from mol format by OPENBABEL (http://www.vcclab.org/lab/babel/). Furthermore, B–DNA dodecamer d(CGCGAATTCGCG)$_2$ crystal structure (PDB ID: 1BNA) was taken from protein data bank (http://www.rcsb.org./pdb). All computation studies were conducted on Intel Pentium 4 operating system having a 2.4 GHz based system containing running MS Windows XP SP2. Finally, the insight view of docked pose model was visualized by using two molecular graphics programs i.e. CHIMERA (http://www.cgl.ucsf.edu/chimera/).

3. Results and discussion

New metal-based molecular modalities **1–4** were obtained, followed by the stoichiometric addition of new (E)–2–(((5H–[1,2,4]triazino[5,6–b]indol–3–yl)imino)methyl)phenol ligand **L** and 2,2′–Bipyridine/1,10 phenanthroline to Ni(II)/Cu(II) metal sulfates (Scheme 1). Proposed structures of the complexes were established by CHN analysis and various spectroscopic methods. In complexes **1** and **3** displayed square planar geometry, whereas complexes **2** and **4** acquired octahedral environments and were stable toward air and moisture. Conductance values of all the complexes suggest their 1:1 electrolytic nature in DMF solution.

3.1. IR spectra

The IR spectrum of ligand **L** and metal complexes **1–4** were recorded in the range of 4000–400 cm^{-1} at room temperature. The IR spectra of the ligand **L** shows a characteristic peak at 1616.56 cm^{-1} for the azomethine ν(C=N) group which was shifted to lower frequencies in metal complexes **1–4** in the range 1599.91–1581.38 cm^{-1} confirming the coordination of azomethine group to the central metal ion [30]. Apart from this ligand **L** also shows a medium intensity broad band at 3430.69 cm^{-1} due to the presence of the ν(O–H) group attached with the salicylaldehyde moiety [31]. However, the absence of this ν(O–H) band in complexes **1** and **3** confirms the coordination by the deprotonation of the hydroxyl group. But in complexes **2** and **4** the broadness and intensity of the ν(O–H) band nearly at ~3429.18 cm^{-1} was increased indicating the presence of coordinated water molecules thus making it difficult to analyze the deprotonation of the hydroxyl group [32]. Furthermore, the band for the ν(N–H) of the triazino[5,6–b]indole ring was observed in the range of 3200.98–3262.28 cm^{-1} in both ligand **L** and metal complexes **1–4** [33]. For the heteroaromatic structures, the ν(C–H) stretching vibrations of the aromatic ring were expected in the region of 3100–3000 cm^{-1}. Therefore, the characteristic ν(C–H) stretching vibration in ligand **L** was depicted at 3197.98 and 3067.66 cm^{-1} [34]. These –C–H stretching vibrations in metal complexes **1–4** were shifted at 3078.14, 3050.21, 3054.01, 3056.98 cm^{-1}, respectively. Moreover, the peaks in the region 1099.08–1164.69 cm^{-1} were assigned to the ν(C–H) in–plane bending mode of vibration. Similarly strongly intense ν(C–H) out–of–plane bending vibrations were observed in the 751.60–856.77 cm^{-1} range in ligand **L** and metal complexes **1–4**. The other aromatic ring stretching vibrations of the ν(C=C) bond of medium intensity were found at 1537.86 cm^{-1} for ligand **L** and 1537.86–1603.08 cm^{-1} for metal complexes **1–4**. The ν(C–O) stretching vibrations appeared as a sharp peak at 1256.20 cm^{-1} in ligand **L** while in metal complexes the intensity of this peak was expectedly reduced and shifted at 1262.35–1215.95 cm^{-1} [35]. Additionally, in metal complexes **1–4** weak intensity peaks in the range 417.19–427.92 cm^{-1} and 523.16–520.13 cm^{-1} were assigned to the ν(M–N) and ν(M–O) vibrations, respectively, confirming the formation of complexes [36,37].

3.2. NMR spectral studies

The ^{1}H NMR spectra of the ligand **L** displayed a strong characteristic peak at 8.91 ppm due to the presence of azomethine –HC=N proton thus confirming the formation of ligand **L** [38]. Moreover, the signals at 10.25 ppm were attributed to the –NH groups suggesting the presence of the free –NH in ligand **L** [39]. The upfield shift of the phenolic –OH group signal at 12.57 ppm suggests the existence of the intramolecular hydrogen bonding between the hydrogen atom of the phenolic –OH and the nitrogen atom of the azomethine group [40]. The multiplets in the range of 6.53 to 8.04 ppm corresponds to the combined signals of aromatic hydrogen atoms of both the triazino[5,6–b]indole ring and salicylaldehyde moieties present in ligand **L**. However, in the ^{1}H NMR spectra of complexes **1** and **3** the peak for the azomethine –HC=N proton was slightly shifted downfield at 8.98 and 8.99 ppm, respectively thus suggesting the coordination of N–atom to the metal ion [41]. In contrast, the signal for the –OH group at 12.57 ppm was completely disappeared in both complexes which further confirms the deprotonation of the hydroxyl group and the direct coordination of the –OH group with the metal ion. In addition, the signal for the –NH group present in triazino[5,6–b]indole ring was shifted upfield at 9.50 and 9.57 ppm in complexes **1** and **3**, respectively. Furthermore, the peaks in the aromatic region from 6.78–7.90 ppm and 6.83–7.94 ppm were broad and merged in both complexes **1** and **3**, respectively. The broadness in these signals were observed mainly due to the presence of metal ions, so it is quite difficult to differentiate the signals of the triazino[5,6–b]indole ligand **L** and 2,2′–Bipyridine/1,10 phenanthroline separately in the aromatic region. Additionally, a strong peak at 3.40 ppm in the case of ligand **L** and a very broad peak at 3.44 and 3.37 ppm in complexes **1** and **3** in the ^{1}H NMR spectra suggested the association of water molecules. The strong broadening of the H_2O molecule signal in the case of metal complexes indicates the dynamic processes such as proton exchange or the presence of water molecules in the solvent [42]. On the other hand, a sharp peak observed at 2.51 ppm, 2.45 and 2.49 ppm was due to the presence of DMSO solvent in ligand **L** and complexes **1** and **3**, respectively [43] (Fig. S1).

In the ^{13}C NMR spectra of ligand **L**, a characteristic peak at 164.8 was observed for the azomethine carbon atom. The resonance signals for the aromatic triazino[5,6–b]indole ring was found in the range of 109.99–153.4 ppm [44]. The signals for the carbon atoms of the aromatic salicylaldehyde ring were observed in the 116.12–133.66 ppm range except for the carbon atom that is bonded to the –OH group which was observed at 161.36 ppm [45]. However, in complexes **1** and **3** the azomethine carbon was shifted downfield at ~173 ppm suggesting the formation of complexes [46]. The resonance signals for the aromatic carbon atoms of ligand **L** were assigned in the range 110.21–160.74 ppm. The characteristic signatures for the aromatic 1, 10 phenanthroline ring were identified in the 126.25–156.01 ppm range [47].

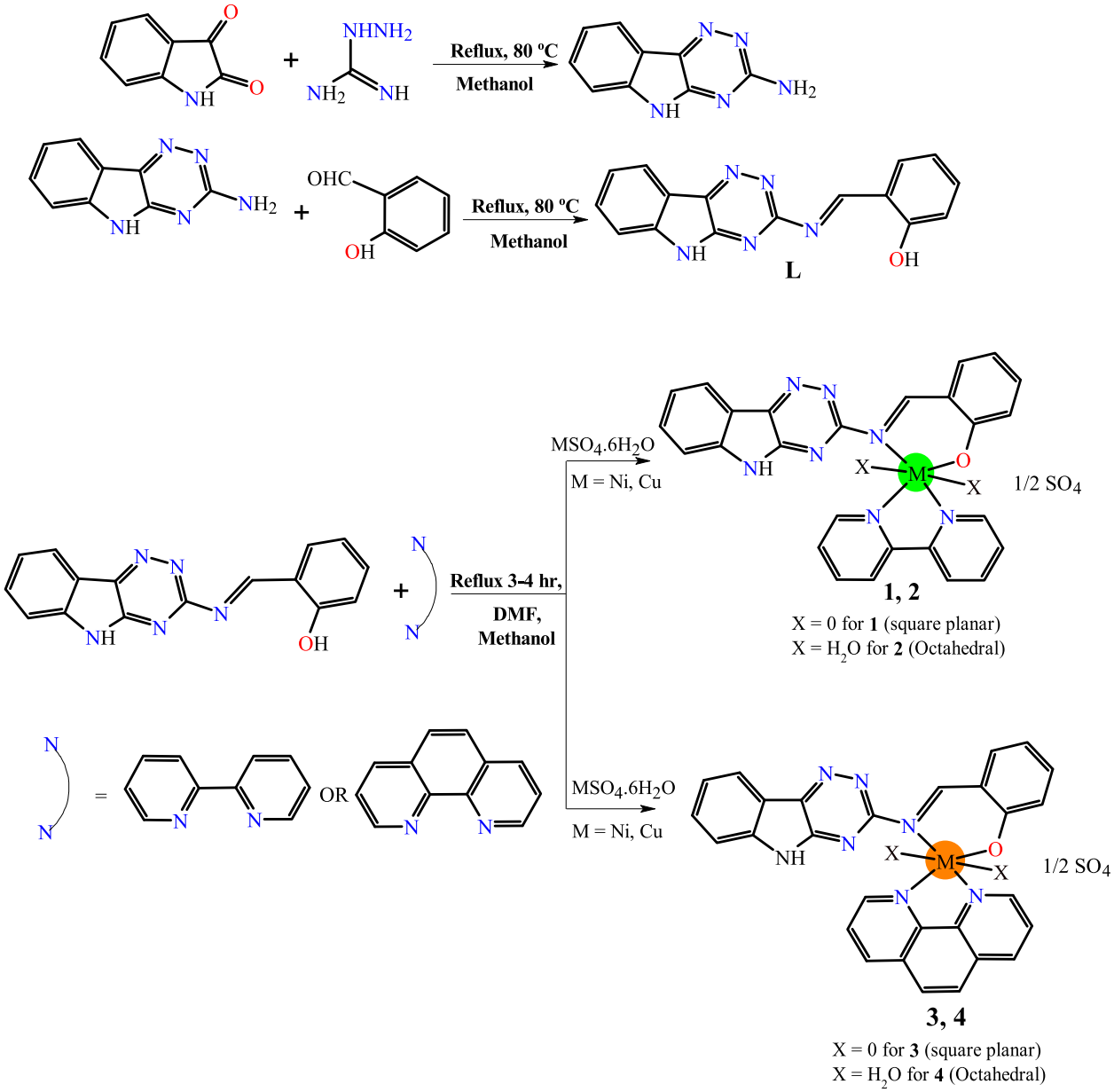

Scheme 1. Synthetic route to ligand **L** and metal complexes **1**–**4**.

3.3. Electronic spectra

The UV–vis spectra of the ligand **L** and the metal complexes **1**–**4** were measured in a DMF solution (10^{-3} to 10^{-4} M) in the range of 200 to 800 nm at room temperature. The ligand **L** exhibited two strong intensity peaks at 280 and 320 nm mainly attributed to the intraligand transitions π –$\pi^*$and n–π^* of the heterocyclic aromatic framework and non-bonding electrons of the nitrogen atom of –C=N groups attached with the triazino[5,6–b]indole moiety, respectively [48,49]. Similarly, the electronic spectra of complexes **2** and **4** displayed an intense absorption band in the range 280–285 nm with a shoulder at 300–320 nm, respectively, affirming the presence of ligand **L** in metal complexes. At higher concentration complex **2** and **4** shows two low energy d–d bands centered at 600,680 nm and 635,695 nm, respectively corresponding to the $^2Eg \rightarrow {}^2T_2g$ transitions suggesting the tetragonally distorted octahedral geometry around Cu(II) ion attributed to the John–Teller effect [50]. However, a shoulder band at 490 and 492 nm in the electronic spectra of complexes **2** and **4**, respectively were assigned to the combination of LMCT (N→ Cu^{2+}) and $^2Eg \rightarrow {}^2T_2g$ transitions [51]. In addition, the effective magnetic moment of complex **4** was calculated from the magnetic susceptibility by using the equation $\mu_{eff} = 2.828\ [\chi_m.T]^{1/2}$ where χ_m is the molar susceptibility and T is the absolute temperature. For complex **4** the magnetic moment was obtained to be 1.92 B.M which is slightly higher than the theoretical value (i.e 1.73 B.M) thus indicating the monomeric nature and octahedral geometry of Cu(II) complex [52]. Unfortunately, the magnetic moment value of complex **2** cannot be recorded due to the slight hygroscopic nature of the complex. On the other hand, the Ni(II) complexes **1** and **3** exhibited a high intensity band at 275–281 nm, respectively and a slight shoulder at 325–319 nm which is more pronounced in the case of complex **3** [53]. Apart from this, a strong peak at 480 nm at higher concentrations in complexes **1** and **3** corresponds to the LMCT transitions. Complex **1** exhibited two absorption bands at 535 and 620 nm whereas complex **3** shows the bands at 550 and 625 nm corresponding to the

spin forbidden $^1A_1g \rightarrow {}^1A_2g$ and $^1A_1g \rightarrow {}^1B_1g$ transitions characteristic of the square planar Ni(II) complexes. Furthermore, very low magnetic susceptibility values in complexes **1** and **3** suggested the diamagnetic nature of Ni(II) complexes consistent with the square planar arrangement.

3.4. Thermal gravimetric analysis (TGA)

To determine the thermal stability of metal complexes **1**–**4**, the TGA analysis has been carried out over the temperature range of 25–800 °C (Fig. S3). In complex **1**, the decomposition of the complex occurs in four steps in the temperature range of 85.72–159.96, 159.96–223.43, 223.43–464.93, 464.93–690.92 °C. However, in complexes **2**–**4**, the weight loss has been observed in three steps over the temperature range of 94.03–206.23, 176.77–395.54, 539.64–652.64 °C. In the case of complexes **1** and **3**, a loss of sulfate molecules accompanied by a % weight loss of 7.37% and 7.03% (calculated%: 8.71 and 8.34) was observed in the first step in temperature range 85.72–159.96 and 108.76–206.23 °C, respectively. In the second step in complex **1** (159.96–223.43 °C), there was the elimination of CO_2 from the molecule with a weight loss of 7.88% (calculated%: 8.74) whereas in complex **3** (206.23–395.54 °C) there is a weight loss of 18.43% (calculated%: 19.93) corresponding to the removal of salicylaldehyde moiety. However, in complex **1** (223.43–464.93 °C) the decomposition of salicylaldehyde moiety occurs in the third step assigned to the weight loss of 26.71% (calculated%: 25.94). In the last step in complexes, **1** and **3**, the weight loss of 19.22% and 20.60% (calculated%: 19.20 and 20.30) in the temperature range 395.54–690.92 °C, respectively were assigned to the further decomposition of organic ligand leading to the generation of NiO as final residue. Similarly, in complexes **2** and **4** (94.03–176.77), there is a loss of two coordinated water molecules causing a weight loss of 6.76% and 5.63% (calculated%: 6.08 and 5.84), respectively. In the second step in complex **2** (201.57–263.46 °C) there is a weight loss of 16.20% (calculated%: 16.56) due to the elimination of sulfate ion and CO_2 molecule while in complex **4** (176.77–342.04 °C), a greater weight loss of 37.41% (calculated%: 36.40) was observed which indicated the removal of sulfate ion, CO_2 and salicylaldehyde moiety from the molecule. In the third step in the temperature range of 263.46–634.45 °C in complexes **2** and **4** there is a decomposition of the remaining organic ligand accompanied with weight loss of 40.64 and 20.52% (calculated%: 40.08 and 20.12), respectively ultimately forming the CuO at the end.

3.5. Mass spectra

The ESI mass spectra of ligand **L** and metal complexes **1**–**4** exhibited a prominent molecular ion peak at 290.3, 552.03, 595.51, 576.34, and 617.43, respectively in support of our chemical structures. In the case of metal complexes **1**–**4**, the loss of the counter ion ($1/2SO_4^{2-}$) is observed leading to the formation of complex ion observed at m/z 504.16, 543.99, 528.31 and 568.43, respectively. In complexes **1** and **3**, the complex ions $[C_{26}H_{18}N_7NiO]^+$ and $[C_{28}H_{18}N_7NiO]^+$ were further fragmented giving peaks at m/z 346.10 and 346.35 corresponding to the $[C_{26}H_{18}N_7NiO–C_{10}H_8N_2]^+$ and $[C_{28}H_{18}N_7NiO–C_{12}H_8N_2]^+$ fragments indicating the removal of bipyridine and phenanthroline, respectively. The peaks at 289.10 and 289.62 were ascribed to $[C_{26}H_{18}N_7NiO–C_{10}H_8N_2–Ni]^+$ and $[C_{28}H_{18}N_7NiO–C_{12}H_8N_2–Ni]^+$ fragments clearly showing the separation of nickel metal ion leaving behind the Schiff base ligand **L**. Similarly in complexes **2** and **4** the resulting loss of the sulfate counter ion in the first step give rise to the complex ions $[C_{26}H_{22}N_7CuO_3]^+$ and $[C_{28}H_{22}N_7CuO_3]^+$ appearing at m/z 543.20 and 568.43 in the mass spectra. In the second step, there will be loss of both water molecules from complexes **2** and **4** correspondings to the $[C_{26}H_{22}N_7CuO_3–2H_2O]^+$ and $[C_{28}H_{22}N_7CuO_3–2H_2O]^+$ observed at m/z 507.20 and 532.36, respectively. In the next step, there will be complete removal of bipyridine/phenanthroline ligands as evidenced from the appearance of peaks at m/z 351.10 and 351.64 corresponding to $[C_{26}H_{22}N_7CuO_3–2H_2O–C_{10}H_8N_2]^+$ and $[C_{28}H_{22}N_7CuO_3–2H_2O–C_{12}H_8N_2]^+$ fragments. After this, the copper metal ion is lost giving a peak at nearly m/z 288 in both complexes **2** and **4** attributed to the $[C_{26}H_{22}N_7CuO_3–2H_2O–C_{10}H_8N_2–Cu]^+$ and $[C_{28}H_{22}N_7CuO_3–2H_2O–C_{12}H_8N_2–Cu]^+$ fragments, respectively. Moreover, in ligand **L** and metal complexes **1**–**4** high intensity peaks were seen at m/z 185 and 106 due to the presence of indole triazine and salicylaldehyde moiety, respectively. Therefore, in the metal complexes **1**–**4**, the complex ions are the main species responsible for the interaction with DNA and HSA as the counter ion is very easily lost in the first step of the mass fragmentation process.

3.6. DNA binding studies

3.6.1. Electronic absorption titration

The DNA binding interaction of ligand and metal complexes was commonly studied by employing the electronic absorption technique. The electronic absorption spectra were evaluated for the ligand **L** and complexes **1–4** by monitoring the changes in the maximum absorption band at 271 nm assigned to the intraligand $\pi \rightarrow \pi^*$ transitions of the aromatic rings [54,55]. Moreover, a very weak band nearly in the region of 330–360 nm in ligand **L** and complexes **2**–**4** was attributed to the $n \rightarrow \pi^*$ transitions of the heterocyclic rings. When a complex is bound to DNA, either hypochromism or hyperchromism was observed with or without any red or blue shift in the position of the absorption band. The hypochromism mainly represents the stacking of the aromatic planar residues inside the base pairs of the DNA helix thereby showing the intercalative binding mode. However, hyperchromism was associated with the electrostatic interaction of the molecule with the sugar phosphate backbone and the stabilization of the DNA secondary structure. The absorption spectra of ligand **L** and complexes **1–4** in the absence and presence of DNA in 5mM Tris HCl/NaCl buffer were depicted in Fig. 1. The incremental addition of DNA concentration to a constant volume of ligand **L**, metal complexes **1** and **2** shows hyperchromism of 44.2%, 91.5% and 67.85%, respectively in the absorption profile with a slight red shift of 3–5 nm in **1** and **2** in the range 265–271 nm. The spectral characteristics such as red shift and hyperchromic effect suggested both covalent binding *via* the N7 atom of guanine and non–covalent binding mode through the breakage of hydrogen bonds between the DNA base pairs leading to the overall contraction and stabilization of the DNA secondary structure [56]. Similarly, hyperchromism of 45.97% and 73.91% was also observed in the absorption profile of complexes **3** and **4,** respectively but with a strong blue shift of 6–9 nm in the maximum absorption band. The concomitant blue shift along with hyperchromism in the absorption intensity inferred the interaction of metal complexes with DNA through the groove binding or external contact by electrostatic interaction with the phosphate backbone of the DNA helix [57,58]. In order to access the binding propensity of ligand and metal complexes, the intrinsic binding constant K_b was quantitatively determined by using the Wolfe–Shimer Eq. (1). The value of K_b evaluated from the ratio of slope to intercept in a plot of [DNA]/($\varepsilon_a - \varepsilon_f$) Vs [DNA] follows the order **4>3>2>1>L** (Table 1). These results revealed that all metal complexes **1**–**4** exhibited higher binding constant K_b values as compared to the ligand **L** and thus we can say that complexation of organic ligands with metal ions increases the binding ability thereby acting as stronger DNA binding agents. Finally, it can be concluded that hyperchromism in the absorption spec-

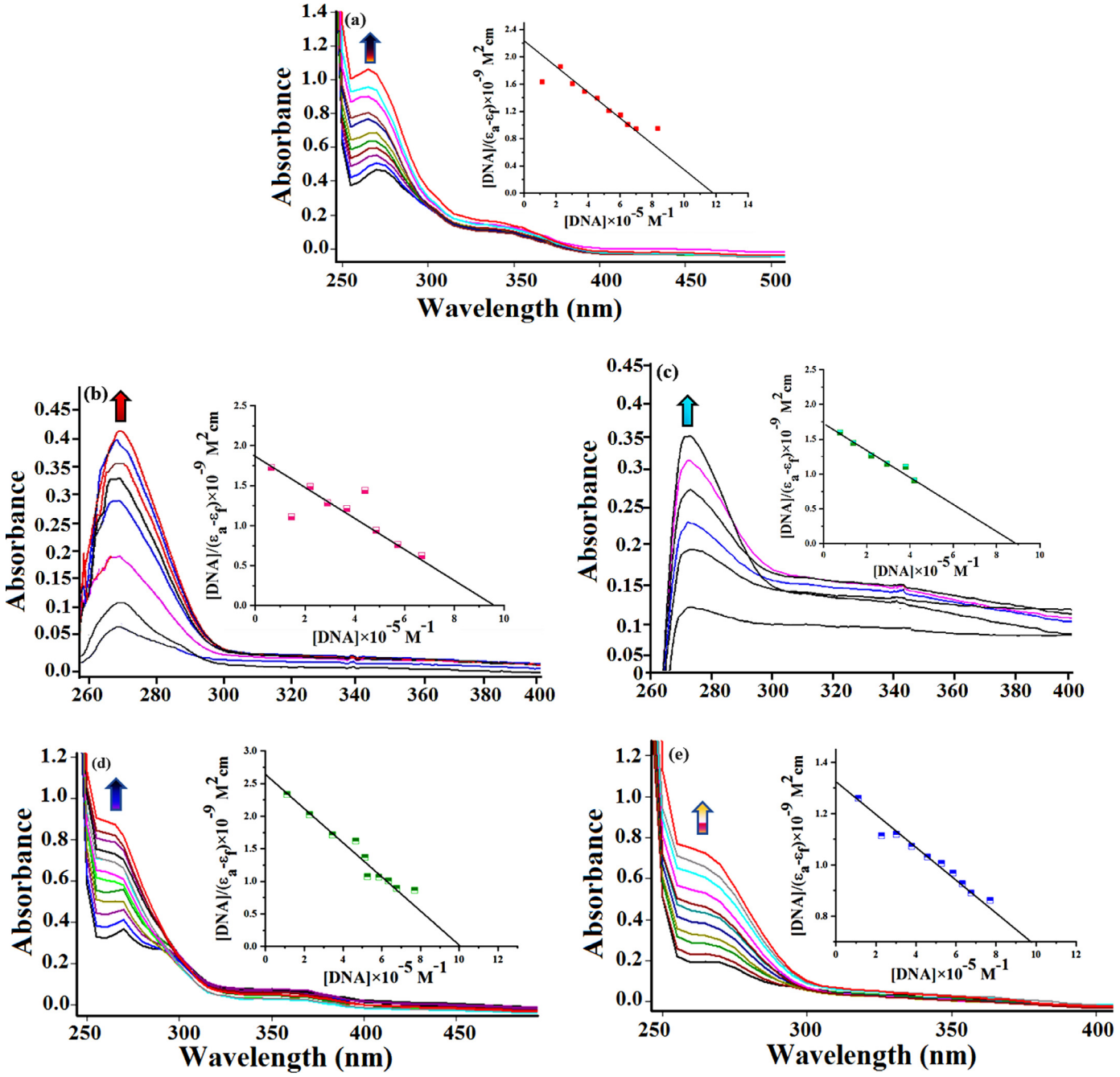

Fig. 1. Absorption spectra of ligand **L** and metal complexes **1**–**4** in 5mM Tris HCl/ 50 mM NaCl buffer upon the addition of calf thymus DNA; Inset: Plots of [DNA]/(ε_a–ε_f) vs [DNA] for the titration of CT DNA with complexes, experimental data points; full lines, linear fitting of the data. [Complex] = 6.42 × 10^{-6} M, [DNA] = 1.14 × 10^{-4} M. Arrow shows a change in intensity with increasing concentration of DNA.

Table 1
DNA binding parameters of ligand **L** and metal complexes **1**–**4** obtained from the electronic absorption studies.

Complex/Ligand	λ_{max} (nm)	$\Delta\lambda$ (nm)	% Hyperchromism	K_b (M^{-1})
L	271	6 (Blue)	44.2%	8.45 × 10^3
1	265	5 (Red)	91.5%	1.04 × 10^4
2	275	3 (Red)	67.85%	1.14 × 10^4
3	269	9 (Blue)	45.97%	1.9 × 10^4
4	265	6 (Blue)	73.91%	4.8 × 10^4

tra in both ligand metal complexes was mainly attributed to the non–covalent electrostatic binding and groove binding through the formation of hydrogen bonds with the –OH and –NH group of the ligand **L** with the accessible hydrogen bonding sites present in the major and minor grooves. However, Cu(II) complexes **2** and **4** exhibited greater binding affinity when compared to their corresponding analogs Ni(II) complexes **1** and **3**. The higher binding propensity of complexes **2** and **4** is mainly due to the presence of selective Cu(II) endogenous metal ion which acts as a promising alternative to platinum-based drugs because it is highly selective towards N7 of guanine residue and strongly interacts with cancerous DNA thereby blocking the uncontrolled replication of DNA which ultimately leads to cell death [59]. Apart from this, Cu(II) is an essential metal ion that is present at the active site of various proteins/enzymes which is involved in many important biological processes in the human body such as respiration, electron transfer, energy metabolism and DNA synthesis [60]. Additionally, the geometry of metal complexes plays a key factor in determining the binding affinity of metal complexes. The literature revealed that octahedral geometry of copper(II) complexes containing aromatic ligands [61,62] are quite fluxional and labile that allows the intercalation of complex inside the DNA base pairs making it a more suitable DNA probe for the development of novel chemotherapeutic agents [63,64].

3.6.2. Fluorescence spectral studies

Fluorescence spectroscopy is one of the most sensitive and accurate techniques to determine the mode of binding of molecules with DNA. The fluorescence emission spectra of ligand **L** and complexes **1–4** exhibited a strong emission band in the range 364–376 nm when excited at a maximum wavelength of 265–275 nm in 0.01 Tris–HCl/50 mM NaCl buffer at room temperature. The fluorescence titration studies of ligand **L** and complexes **1–4** have been performed in the absence and presence of CT DNA (1.10×10^{-4} M). The changes in the fluorescence intensity and difference in the wavelength shift determine the mode of binding of these complexes with CT DNA. As depicted in Fig. 2, the ligand **L**, complexes **3** and **4** show an increase in the fluorescence intensity in the emission peak at 380 nm on continuous addition of increasing concentration of CT–DNA to a constant volume of complex **1.** The complexes **3** and **4** exhibited 43.84% and 51.01% hyperchromism at a ratio of [DNA]/[complex] is 2.4, respectively with a slight blue shift of 2–3 nm (Fig. 2). However, the ligand **L** only shows hyperchromism with no shift in the position of the emission peak. The enhancement in the emission intensity and red/blue shift indicates the electrostatic interaction of complexes **3** and **4** towards the negatively charged phosphate backbone of DNA [65]. This type of behavior was also expected due to the highly planar structure of the phenanthroline present in complexes. Furthermore, the increase in the emission intensity is the characteristic of intercalator molecules; therefore our complexes **3** and **4** due to the presence of highly planar phenanthroline ring will also undergo partial interaction inside the adjacent base pairs of DNA helix. This will lead to a decrease in the collisional frequency due to the less accessibility of solvent molecules at the binding site thus proving a hydrophobic environment around the complex molecule [66]. However, in the case of complexes, **1** and **2**, quenching in the intrinsic fluorescence by 11.29% and 19.88% with a red and blue shift of 3 and 5 nm, respectively was observed in the emission peak appearing at 364 nm on incremental addition of CT DNA. This quenching in the fluorescence intensity can be either static quenching or dynamic quenching. The static quenching represents the formation of the ground state complex between the fluorophore and quencher whereas dynamic quenching refers to the interaction of the quencher with a molecule in the excited state [67,68].

Moreover, the binding constant 'K' and number of binding sites 'n' for ligand **L** and complexes **1–4** were calculated from slope and intercept of the Scatchard plot of r/C_f versus r, respectively. The binding constant values follow the order **4>3>2>1>L** in agreement with electronic absorption studies (Table 2). This result indicated the structure–activity relationship in complexes and reveals that the nature of the metal ion and the increase in molecular planarity of the ligands can affect the binding propensity of metal complexes with CT DNA.

3.6.3. Ethidium bromide displacement experiment

An ethidium bromide displacement experiment was carried out to further get detailed insight into the intercalative behavior of complexes with DNA. The ethidium bromide (EB) is basically a sensitive fluorescent probe that emits fluorescence in the presence of DNA; this is due to its highly planar aromatic structure that easily intercalates inside the stacked base pairs of the DNA helix [69]. This staking interaction of EB dye with DNA leads to a very high emission intensity due to the decrease in the quenching effect by solvent molecules. However, the emission intensity of this EB dye decreases when replaced by another molecule at the same intercalating site. Therefore, any molecule that replaces this dye will have the intercalating mode of binding depending upon the ability of intercalation and hence reflected by a decrease in emission intensity [70]. The emission spectra of EB dye show an intense emission peak at 595 nm when excited at 525 nm wavelength in the presence of the DNA molecule, thereby confirming the formation of DNA–EB adducts. As shown in Fig. 3, the increasing concentration of ligand **L** and metal complexes **1–4** quenches the emission intensity of DNA–EB adducts [71]. The results revealed only quenching of the fluorescent intensity with no shift in the position of the band. In both ligand and metal complexes, since EB was not completely displaced from its binding site, it can be concluded that our molecule competes with EB for its binding site and undergo partial intercalation [72]. Therefore, quenching in the fluorescence indicates the partial intercalative behavior of both ligand **L** and metal complexes **1–4**, but the extent of intercalative nature was determined from the quenching constant K_{sv} by using the Stern–Volmer Eq. (1). The quenching constant was calculated from the slope of the plot of I_o/I verses [Complex] follows the order **4>3>2>1>L** (Table 3). Furthermore, the apparent binding constant K_{app} values at the 50% quenching of the fluorescent intensity of DNA–EB adduct by ligand **L** and metal complexes **1–4** were calculated by using the equation [73]: $K_{app} \times [\text{ligand/complex}]_{50} = K_{EB} \times [EB]$, where $[\text{ligand/complex}]_{50}$ is the concentration of molecule at 50% quenching, K_{EB} is the binding constant of Ethidium bromide ($K_{EB} = 1.0 \times 10^7$ M^{-1}) and [EB] is the concentration of ethidium bromide (3.33×10^{-6} M) [74]. The K_{app} values for ligand **L** and metal complexes **1–4** are mentioned in Table 3. These K_{sv} and K_{app} values suggested that complex **4** has a stronger ability to intercalate partially inside the DNA helix as compared to the other complexes and ligands alone.

3.7. HSA binding studies

3.7.1. Absorption spectral studies

To investigate the changes in the secondary structure of HSA on interaction with ligand/ complexes, electronic absorption studies were conducted under physiological conditions. The electronic absorption spectrum of HSA shows a strong peak at 280 nm due to the tryptophan amino acid residues present in HSA. It is well established in the literature that any changes in the absorption spectra of HSA were mainly due to the formation of the ground state complex and unfolding of the polypeptide chain thus supporting the static fluorescence quenching mechanism. However, the dynamic quenching only affects the excited state of the molecule

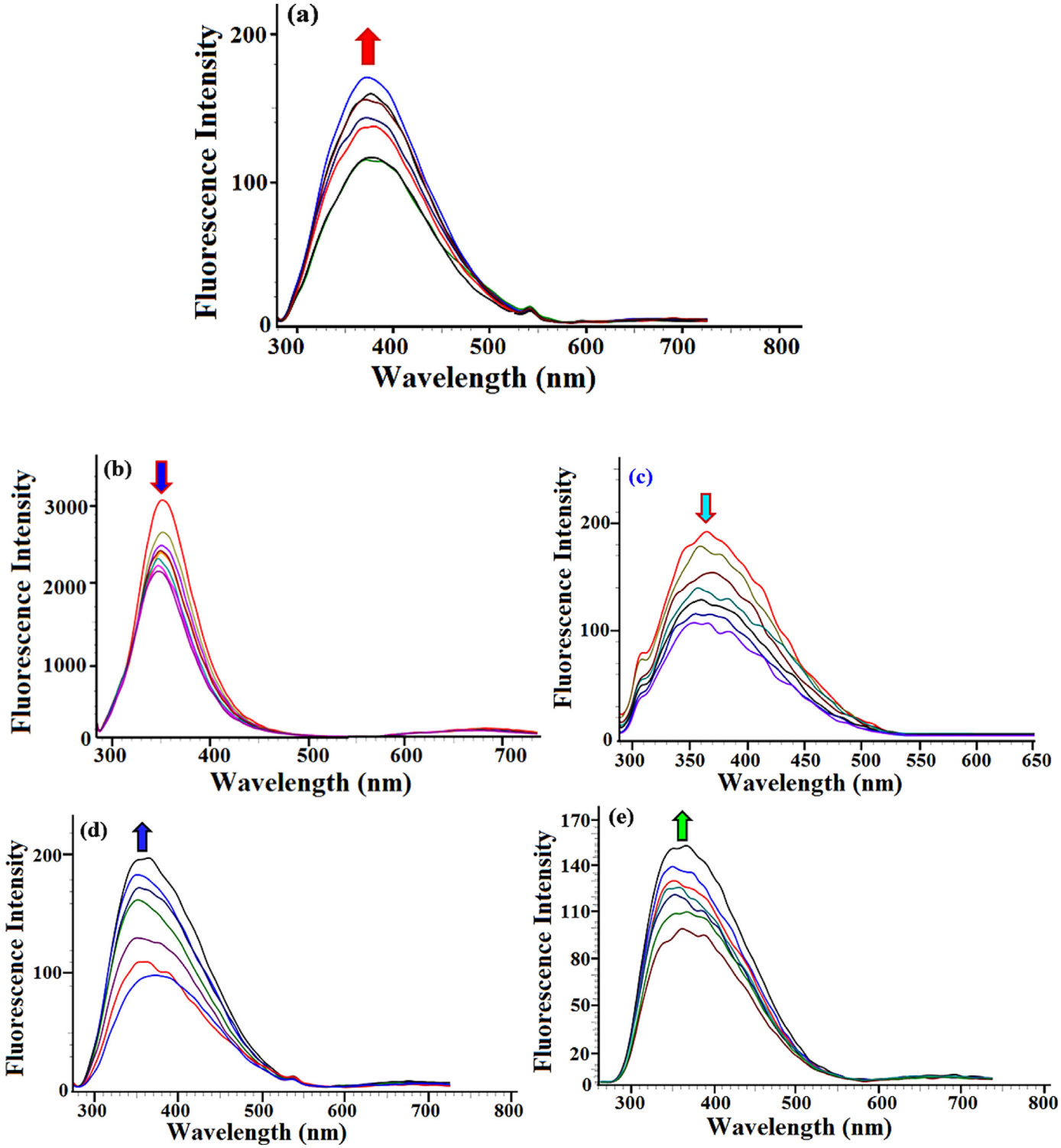

Fig. 2. Emission spectra of ligand **L** and metal complexes **1–4** in Tris–HCl buffer (pH 7.3) in the presence and absence of CT DNA at room temperature. The arrow shows a change in intensity with the increasing concentration of DNA.

Table 2
DNA binding constant (K) values, percent hypo–/hyperchromism and shift in the wavelength (Δλ) for the interaction of ligand **L** and metal complexes **1–4**.

Complex/Ligand	Emission wavelength λ_{em} (nm)	Δλ (nm)	% Hypo–/ Hyperchromism	K (M^{-1})
L	376	No shift	3.06%	6.56×10^3
1	364	3 (Red shift)	11.29%	1.81×10^4
2	364	5 (Blue shift)	19.88%	3.03×10^4
3	364	8 (Red shift)	43.84%	6.03×10^4
4	366	9 (Blue shift)	51.01%	7.12×10^4

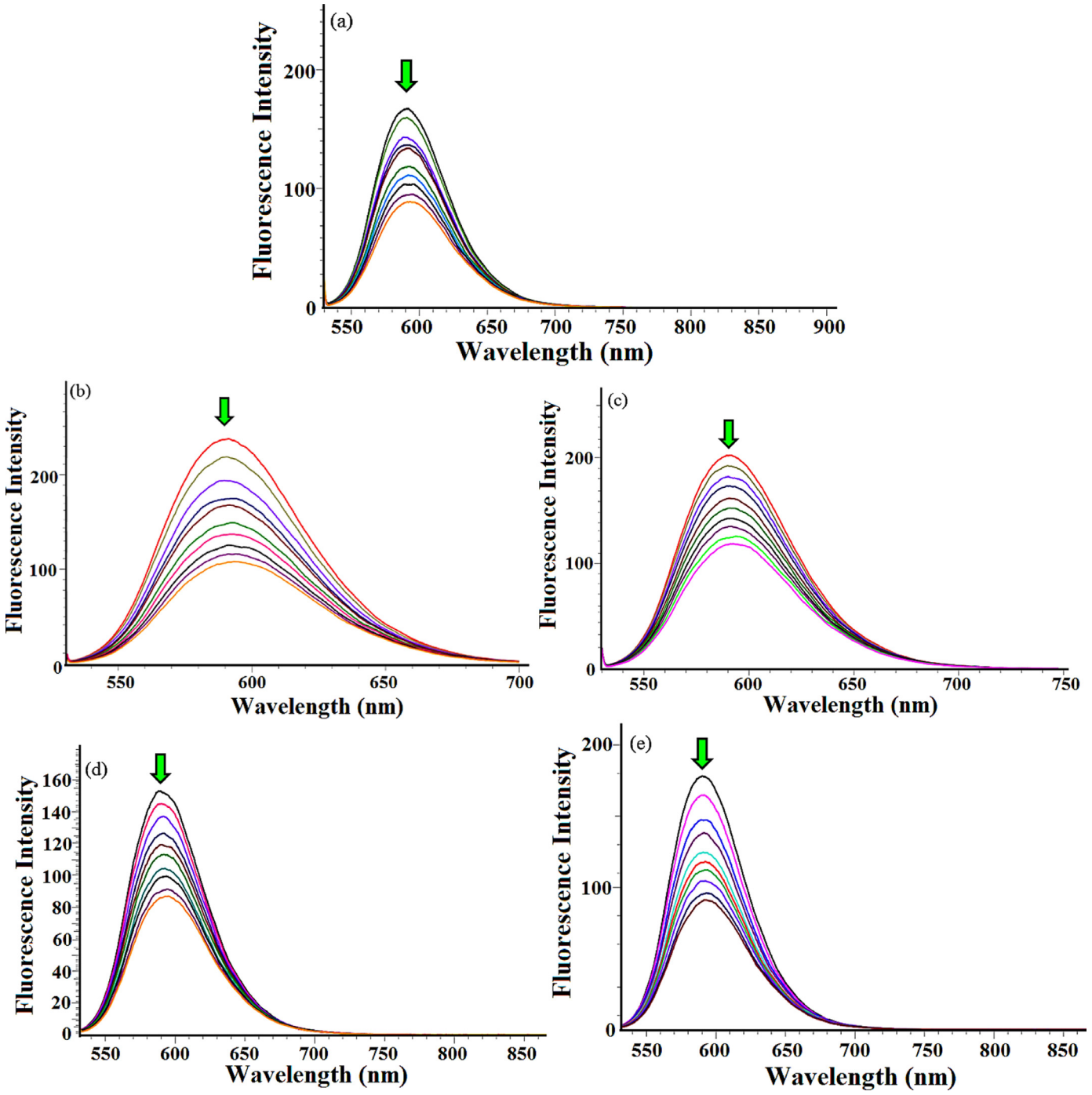

Fig. 3. Emission quenching spectra of CT DNA (1.10×10^{-4} M) bound ethidium bromide (3.33×10^{-5} M) in the presence of ligand **L** and metal complexes **1**–**4** in buffer 5 mM Tris–HCl/50 mM NaCl, pH = 7.2 at room temperature. The arrow depicts a change in intensity with the increasing concentration of dye ethidium bromide.

Table 3
Binding parameters for the competitive ethidium bromide displacement studies for ligand **L** and metal complexes **1**–**4**.

Complex/Ligand	% Hypochromism	K_{sv} (M^{-1})	K_{app}
L	39.61	1.73×10^4	1.08×10^6
1	46.94	2.25×10^4	1.80×10^6
2	41.65	2.50×10^4	1.92×10^6
3	43.04	3.36×10^4	2.01×10^6
4	48.87	4.38×10^4	2.58×10^6

and did not alter the absorption spectra of fluorophore [75,76]. The electronic absorption spectra were recorded of on incremental addition of ligand **L** and complexes **1**–**4** ($0.12–1.26 \times 10^{-5}$ M) to a fixed amount of HSA (2.27×10^{-5} M) in 5 mM Tris– HCl/NaCl buffer at room temperature (Fig. 4). The results revealed hyperchromism in the intensity along with a blue shift of 5 nm in the absorption spectra of complexes **1** and **2** whereas a red shift of 3 nm in the case of complexes **3** and **4**. In contrast, no shift in the wavelength was observed in the absorption profile of HSA showing no alteration in the microenvironment around the tryptophan residue on increasing the concentration of ligand **L** [77]. In complexes **1** and **2**, a substantial increase in the ab-

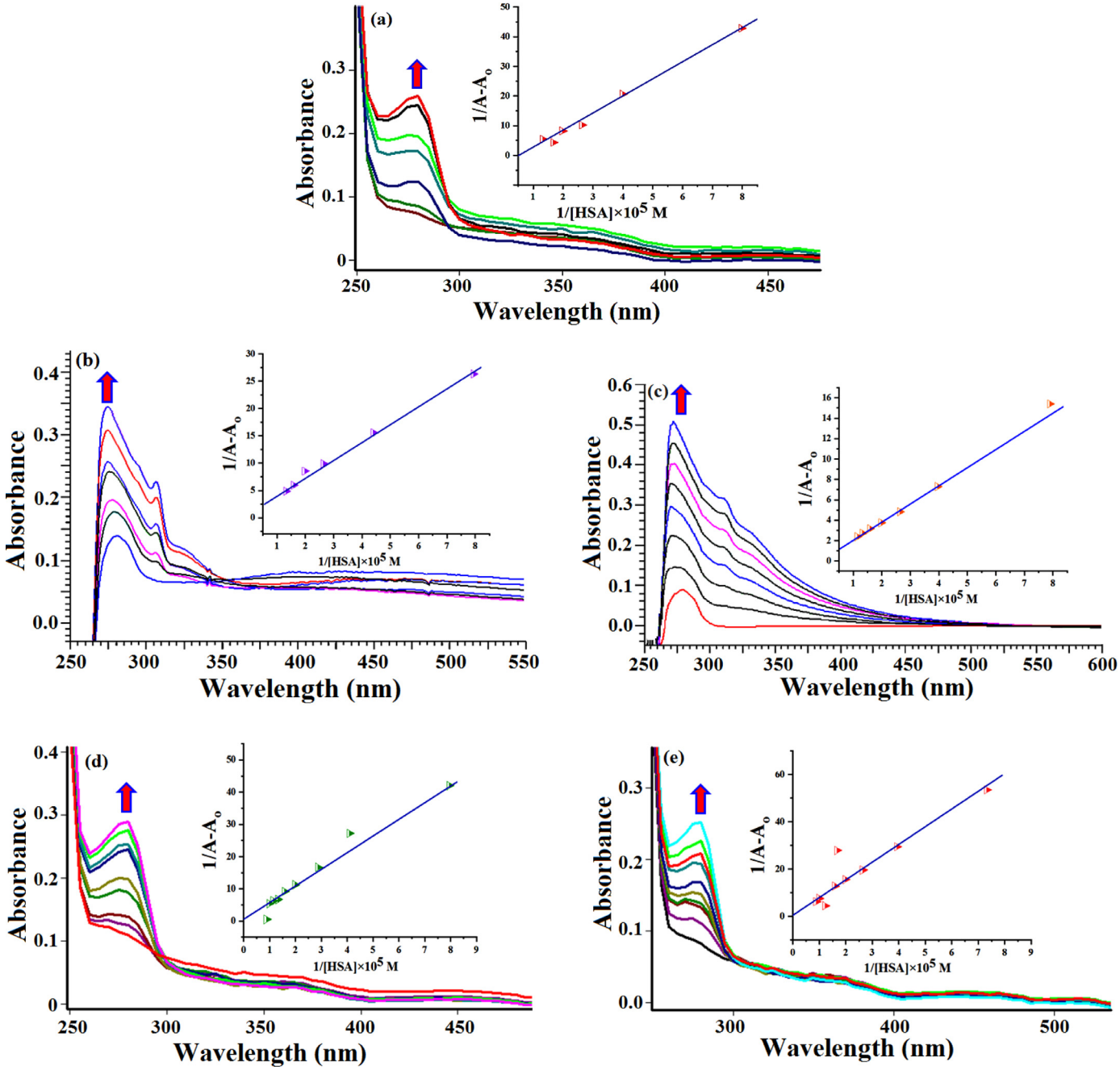

Fig. 4. UV absorption spectra of the ligand **L** and metal complexes **1**–**4** in the presence and absence of HSA in 5 mM Tris– HCl/50 mM NaCl buffer, pH 7.3, at room temperature: [HSA] = 2.27 × 10^{-5} M; [Complex] = 0.12–1.26 × 10^{-5} M. Arrows show the intensity changes upon the increasing concentration of the complex 1. Inset: Plot of 1/A–A_o vs. 1/ [Complex].

sorbance and blue shift in the wavelength indicated an increase in the polarity around the tryptophan residues thereby reducing the hydrophobicity leading to conformational changes in the peptide strands of HSA [78]. Similarly, in complexes **3** and **4**, the marked red shift and hyperchromism also indicated changes in the microenvironment in Trp–214 residue due to the formation of ground state complex with HSA leading to structural changes in the secondary structure of HSA [79,80]. Overall, we concluded that the observed increase in the absorption intensity suggests the non–covalent interaction probably through the formation of hydrogen bond between the complexes and HSA molecule. The intrinsic binding constants (K_b) for the HSA binding of ligand **L** and metal complexes **1**–**4** have been evaluated from the ratio of the intercept to slope from the linear double reciprocal plot of 1/(A–A_o) versus 1/[ligand/complex] by using Eq. (1). The K_b values were found to be 2.36 × 10^3, 1.29 × 10^4, 6.33 × 10^4, 7.32 × 10^4, 8.57 × 10^4 for **L** and complexes **1**–**4**, respectively. These results showed that complexes **2** and **4** containing Cu(II) ions exhibited a stronger binding affinity towards HSA than its analogous Ni(II) complexes **1** and **3**. It can be expected as 15% of the total copper content in blood plasma was transported by HSA under normal conditions. Since HSA acts as a carrier and shows high selectivity towards Cu(II) ions in the human body, therefore, the Cu(II) complexes possess high HSA binding affinity [81]. It is reported that the copper-binding site in the HSA is the amino N-terminal site with the sequence Asp-Ala-His which binds easily to

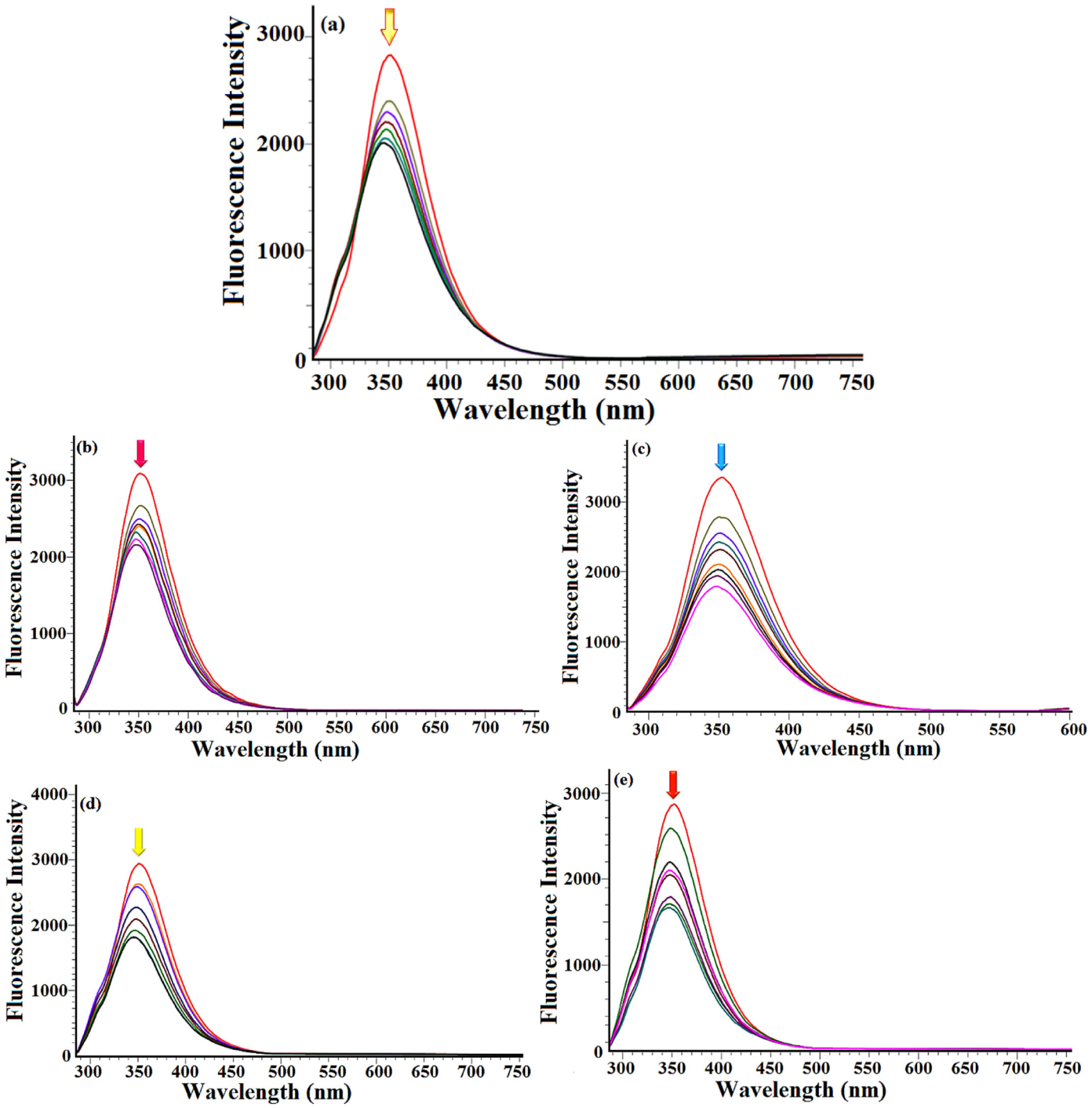

Fig. 5. The fluorescence quenching spectra of HSA in the presence of ligand **L** and metal complexes **1–4** at excitation wavelength at 280 nm in 5 mM Tris–HCl/50 mM NaCl buffer, pH 7.3, at room temperature: [HSA] is 2.27 × 10^{-5} M; the concentration of complex increases from 0.73 × 10^{-6} to 8.06 × 10^{-6} M, respectively. The arrow shows the intensity changes upon the increasing concentration of the quencher at an emission wavelength of 350 nm.

the Cu(II) ion and delivers to the tissues and organs in the human body [82].

3.7.2. Fluorescence quenching studies

The affinity of drug molecules to bind with the carrier protein HSA which is freely accessible inside the blood helps in the distribution, metabolism and pharmacological properties of the blood [83,84]. The binding interaction of ligand/metal complexes with HSA protein was studied by the highly sensitive fluorescence spectroscopy technique. The intrinsic fluorescence of HSA was mainly due to the presence of tryptophan (Trp–214) residue with a substantial contribution from tyrosine (Tyr), and phenylalanine (Phe) residues. The Trp–214 residue is located in the subdomain IIA of HSA which also contains a large hydrophobic cavity near Trp–214 that acts as a binding site for many drugs [85]. The fluorescence spectra of HSA have been recorded in the range of 200–800 nm with excitation wavelength at 280 nm in the absence and presence of an increasing concentration of ligand **L** and metal complexes **1–4** (Fig. 5). The HSA (2.27 × 10^{-5} M) shows a strong emis-

Table 4
The HSA binding constants and parameters derived for ligand **L** and complexes **1–4**.

Compound	K_{sv} (M^{-1})	K_q (M^{-1} s^{-1})	K (M^{-1})	n
L	6.06×10^4	6.06×10^{12}	0.65×10^4	0.82
1	6.22×10^4	6.22×10^{12}	1.11×10^4	1.05
2	9.89×10^4	9.89×10^{12}	1.31×10^4	1.10
3	1.33×10^5	1.33×10^{13}	1.51×10^5	1.38
4	2.50×10^5	2.50×10^{13}	1.72×10^5	1.40

sion peak at 355 nm which was specifically quenched along with the slight blue shift of 5–6 nm on gradual addition of an increasing amount of ligand **L** and metal complexes **1–4** (0.73×10^{-6} to 8.06×10^{-6} M). This quenching in the fluorescence intensity and the blue shift indicates Trp–214 residues are less exposed to the solvent molecules and are buried in the more hydrophobic environment after binding with the ligand/ metal complexes [86]. However, the quenching in the case of complex **4** was more as compared to complex **1, 2, 3** and ligand **L** due to the presence of a highly planar phenanthroline ring causing greater interaction with HSA. The overall results suggest perturbations in the microenvironment around Trp–214 residues leading to the conformational alterations in the secondary structure of HSA [87].

To analyze the quenching mechanism of HSA by ligand **L** and metal complexes **1–4**, the fluorescence data were evaluated by employing the Stern–Volmer Eq. (5):

$$\frac{Fo}{F} = 1 + K_q \tau_o [Q] = \ 1 + K_{SV}[Q] \tag{5}$$

where F_o and F are the emission intensities of HSA in the absence and presence of quencher (ligand/metal complex), respectively, k_q is a bimolecular quenching rate constant of HSA (equal to $K_q = K_{SV}/\ \tau_o$), τ_0 is the average lifetime of fluorophore in the absence of quencher ($\tau_o = 10^{-8}$ s), K_{SV} is the Stern–Volmer quenching constant and [Q] is the concentration of a quencher (ligand/metal complex). The Stern–Volmer quenching constant K_{SV} calculated from the plot of F_o/F verses [Q] follows the order **4>3>2>1>L**. Furthermore, bimolecular quenching rate constant K_q given in Table 4 was calculated from the Stern–Volmer quenching constant K_{sv} by employing the equation $K_q = K_{SV}/\ \tau_o$ and was obtained in the order of magnitude 10^{12} to 10^{13}, which was much greater than the limiting diffusion constant K_{dif} of the biomolecules ($K_{dif} = 2\ .0 \times 10^{10}$ M^{-1} s^{-1}). The greater values of $K_q > K_{dif}$ for ligand **L** and metal complexes **1–4** confirmed that fluorescence quenching takes place through a static quenching mechanism [88,89]. The static quenching supports the formation of the ground state complex between the HSA and ligand **L**/metal complexes **1–4** due to specific interaction in agreement with UV–vis absorption results. For a static quenching mechanism, the binding constant (K) and the number of binding sites (n) can be calculated using the modified Stern–Volmer Eq. (6):

$$\log\left[\frac{F_o - F}{F}\right] = logK + nlog[Q] \tag{6}$$

Where, F_o and F are the fluorescence intensities of HSA in the absence and presence of quencher (ligand/metal complex), K is the binding constant, n is the number of binding sites and [Q] is the quencher concentration (ligand/metal complex). By employing this Eq. (2), a double logarithm regression graph of $\log(F_o - F/F)$ versus log[Q] has been plotted and the binding constant (K) was determined from the intercept and the number of binding sites (n) was calculated from the slope (Fig. 6). The values of K and n for ligand **L** and metal complexes **1–4** are mentioned in Table 4. The binding constant K values were found to be in the appropriable range of 10^4–10^5 M^{-1} indicating the excellent interaction between complex **1–4** and HSA. Moreover, the number of binding sites for ligand **L** and metal complexes **1–4** was found to be in the range 0.82–1.4 revealing that there is only one binding site available for interaction with HSA. The value of binding constant K for all ligand **L** and metal complexes **1–4** are in the optimum range to bind with HSA molecule but quite less than the association constant of non–covalent avidin–ligands bonds ($K \approx 10^{15}$ M^{-1}) [90]. This suggests a possible release of the complex at the target site. The results revealed that among the metal complexes **1–4**, complex **4** shows the greater interaction with HSA due to the presence of Cu(II) metal ion which is well known for its specific interaction and transportation by HSA inside the human body [91,92]. Therefore, the nature of metal ions directly affects the bioactivity of metal complexes together with the coexistence of the synergetic effect of ligand [93].

3.7.3. Forster resonance energy transfer (FRET)

The energy transfer between the donor fluorophore (HSA) and acceptor (metal complexes) was observed due to the significant overlap of the emission spectra of HSA and the absorption spectra of the metal complexes **1–4** (Fig. 7). This non–radiative transfer of energy through intermolecular dipole–dipole is also called the Forster resonance energy transfer (FRET). In general, FRET mainly occurs due to the interaction of the acceptor molecule with donor HSA in the excited state leading to the transfer of energy from donor to acceptor molecule [94]. However, the extent of the energy transfer depends on the amount of overlap between the donor HSA and acceptor metal complexes. For efficient energy transfer between donor and acceptor molecules by FRET mainly three criteria's are required: (a) the donor molecule must have some fluorescence, (b) there must be significant overlap between emission spectra of donor and absorption spectra of acceptor and (c) the distance between donor and acceptor molecule must be less than 8 nm [95]. The efficiency of energy transfer (E) and the distance (r) between the tryptophan residue of donor HSA and acceptor metal complexes were evaluated by employing the Eq. (7):

$$E = 1 - \frac{F}{F_o} = \frac{{R_o}^6}{{R_o}^6 + {r_o}^6} \tag{7}$$

Where F and F_o represent the fluorescence intensity of HSA in the presence and absence of the metal complexes **1–4**, r is the actual distance between the donor HSA and acceptor metal complexes and R_o signifies the critical distance at 50% energy transfer which can be computed from the Eq. (8).

$${R_o}^6 = 8.78 \times 10^{-25} K^2 N^{-4} \varphi J \tag{8}$$

Where K^2 is the spatial orientation factor of the donor and acceptor dipoles depending on their geometry, N is the refractive index of the medium, φ is the donor HSA fluorescence quantum yield and J is the overlap integral of the HSA donor fluorescence and absorption spectrum of acceptor metal complexes calculated by using the Eq. (9).

$$J = \frac{\int_0^\infty F(\lambda)\varepsilon(\lambda)\lambda^4 \Delta\lambda}{\int_0^\infty F(\lambda)\Delta\lambda} \tag{9}$$

Where $F(\lambda)$ is the fluorescence intensity of the HSA donor without acceptor at wavelength λ and $\varepsilon(\lambda)$ is the molar absorption coefficient of the acceptor metal complexes at wavelength λ. In the present circumstances the value of $K^2 = 2/3$, $N = 1.336$ and $\varphi = 0.118$ for HSA. The parameters of the Forster resonance energy transfer (FRET) such as E, J, R_o and r for the interaction of the acceptor metal complexes **1–4** with donor HSA were determined by using Eqs. (1) to (3). The calculated values show that the distance between donor and acceptor 'r' is less than that of the critical distance 'R_o' for all the metal complexes thereby confirming the

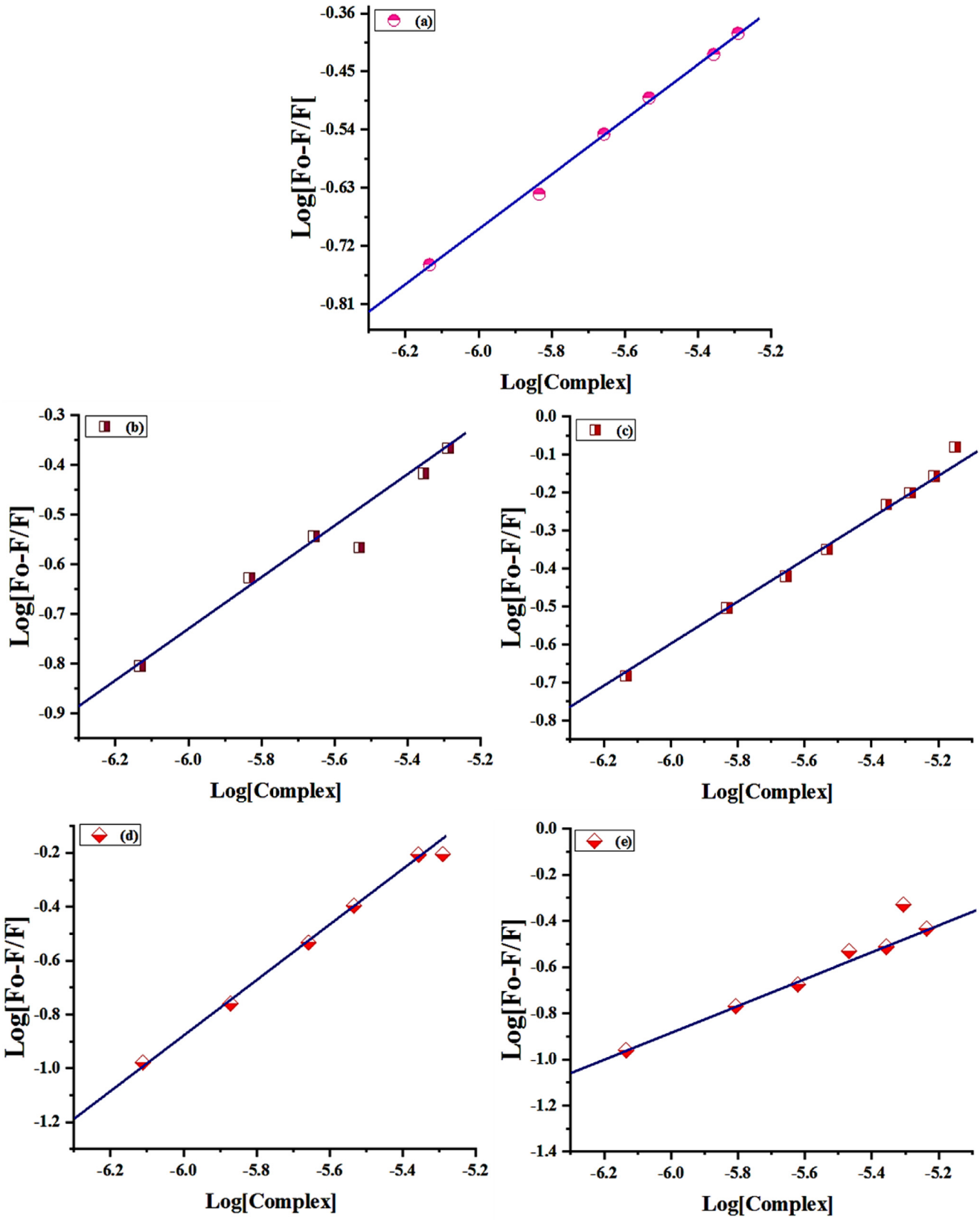

Fig. 6. Double logarithm regression plot of fluorescence quenching of HSA for the calculation of binding constant (K) and the number of binding (n) for ligand **L** and complexes **1**–**4** with HSA at room temperature.

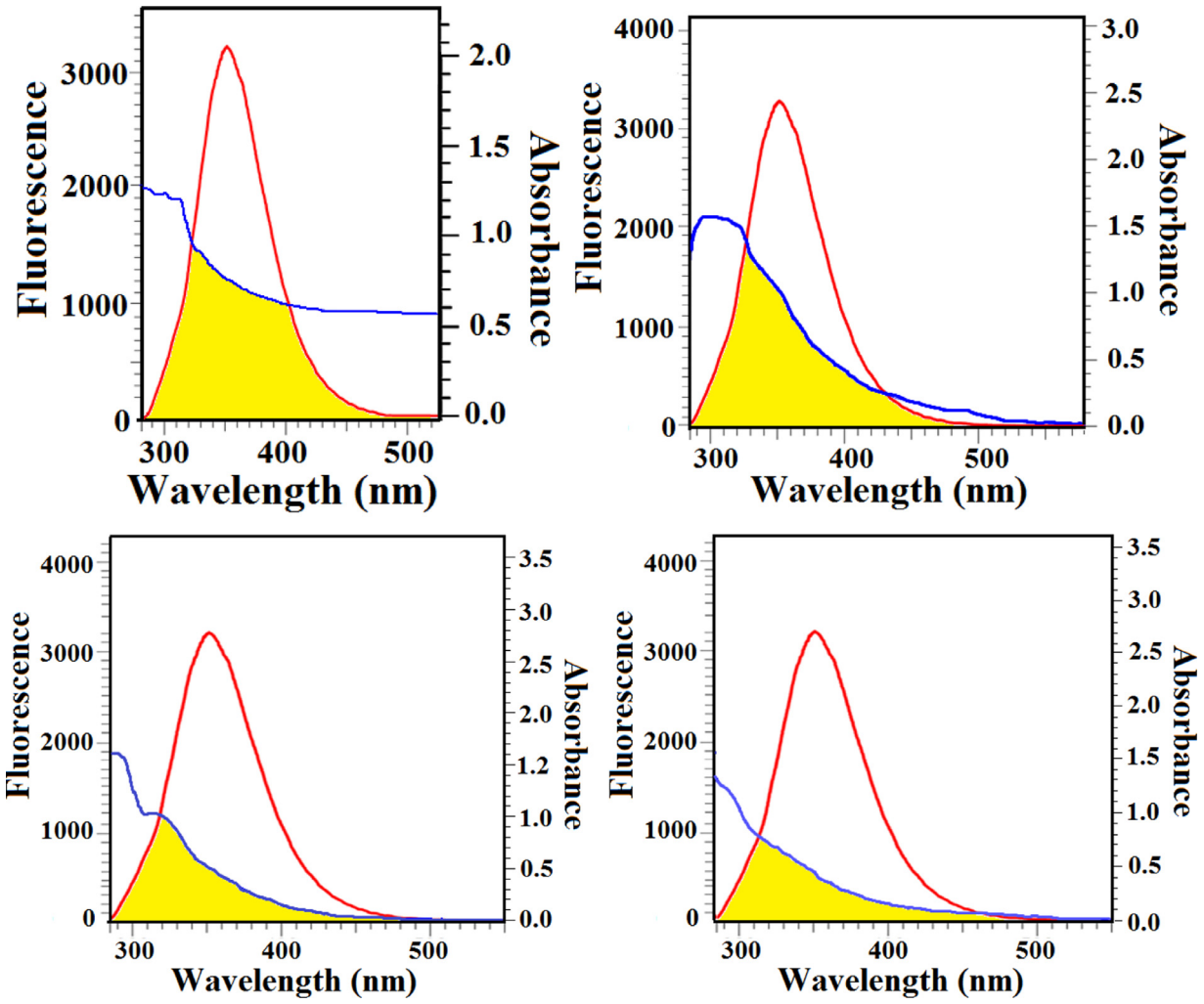

Fig. 7. Spectral overlap (J(λ)) of UV absorption spectra of complexes **1–4** with fluorescence emission spectra of HSA. The red line shows the fluorescence emission spectrum of HSA (0.67×10^{-6} M), the blue line UV absorption spectrum of metal complexes **1–4** (0.67×10^{-6} M).

Table 5
Forster resonance energy transfer (FRET) obtained parameters for energy transfer between HSA and metal complexes **1–4**.

Complex	J (cm³ M⁻¹)	R_o (nm)	E	r (nm)
1	1.27×10^{13}	2.11	0.107	3.12
2	2.18×10^{13}	2.25	0.136	3.13
3	2.48×10^{13}	2.74	0.173	3.14
4	6.07×10^{13}	2.97	0.374	3.17

static quenching mechanism. Moreover, the good value of 'E' revealed the excellent transfer of energy from the tryptophan residue of the HSA to the metal complexes **1–4** along with substantial interaction. For an appropriate energy transfer process the value of r must obey the criteria $0.5R_o < r < 1.5R_o$ which can be simplified in general to $2 < r < 8$ nm [96]. Our all complexes have followed this condition as their r value is observed in the range of 3.02–3.17 nm, therefore, suggesting the exemplary transfer of energy in the order of **4>3>2>1** (Table 5).

3.8. Molecular docking studies with DNA

To further get detailed information on the binding mode of metal complexes with DNA biomolecules, molecular docking studies have been performed for only complexes **3** and **4** due to their higher binding propensity towards DNA. We have performed the rigid molecular docking studies with duplex DNA d(CGCGAATTCGCG)2 dodecamer (PDB ID: 1BNA) to study the binding interaction and proper orientation of our complex at the binding site of the macromolecule [97]. The minimum energy docked poses of our complexes **3** and **4** with DNA revealed that the complex binds in the minor groove in the GC-rich region together with the hydrogen bonding and van der Waal interactions in the groove (Fig. 8). Moreover, the phenanthroline ring bends in such a manner to allow intercalative $\pi-\pi$ stacking interaction with the double helix in agreement with the EB displacement studies [98]. The H–bonding has been observed with the oxygen atom of phenolate and the nitrogen atoms of the triazine ring with the phosphate backbone present in the GC-rich region provides stabilization to the docked pose. Furthermore, the relative binding energy of complexes **3** and **4** in the docked pose of DNA was found to be –6.82 and –7.53 Kcal/mol respectively. The more negative binding energy indicates a more stabilized structure in the docked posed, thus the values of the binding energy evidenced that complex **4** more strongly binds with DNA as compared to complex **3**. This is in agreement with the same order as obtained from the experimental electronic absorption studies. Overall these results are in close correlation with the DNA binding results which confirms the partial intercalation along with groove binding for complexes **3** and **4**.

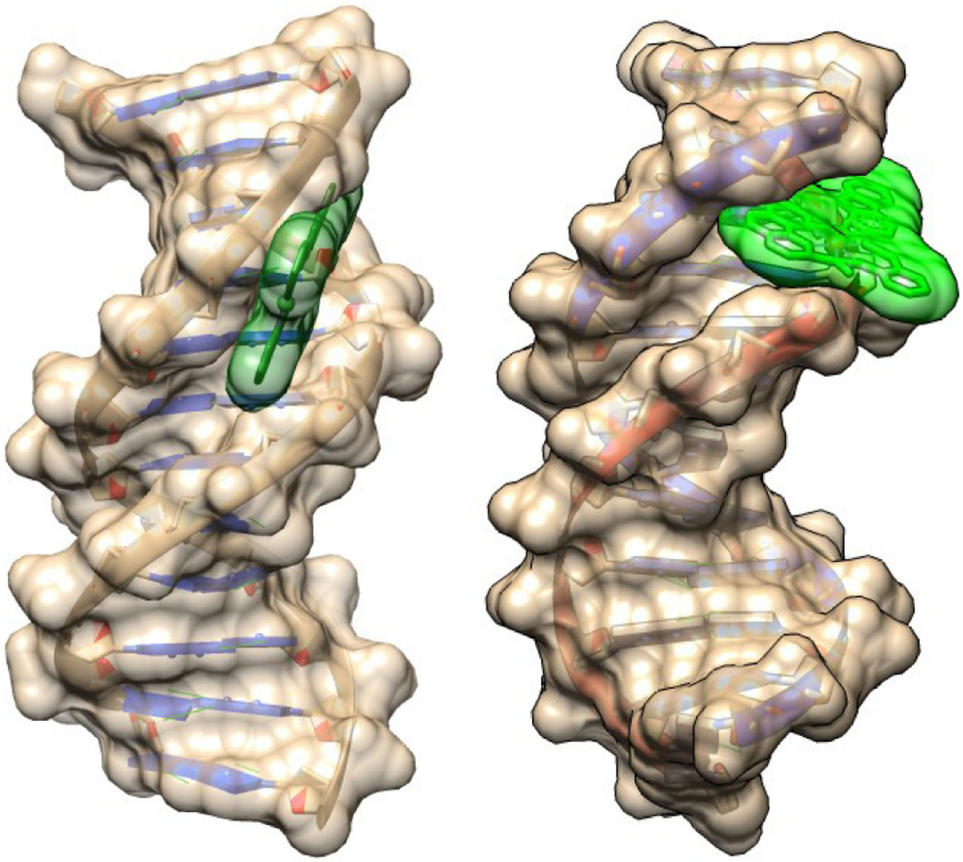

Fig. 8. Molecular docked poses of complex **3** and complex **4** with DNA dodecamer of sequence d(CGCGAATTCGCG)2 (PDB ID: 1BNA).

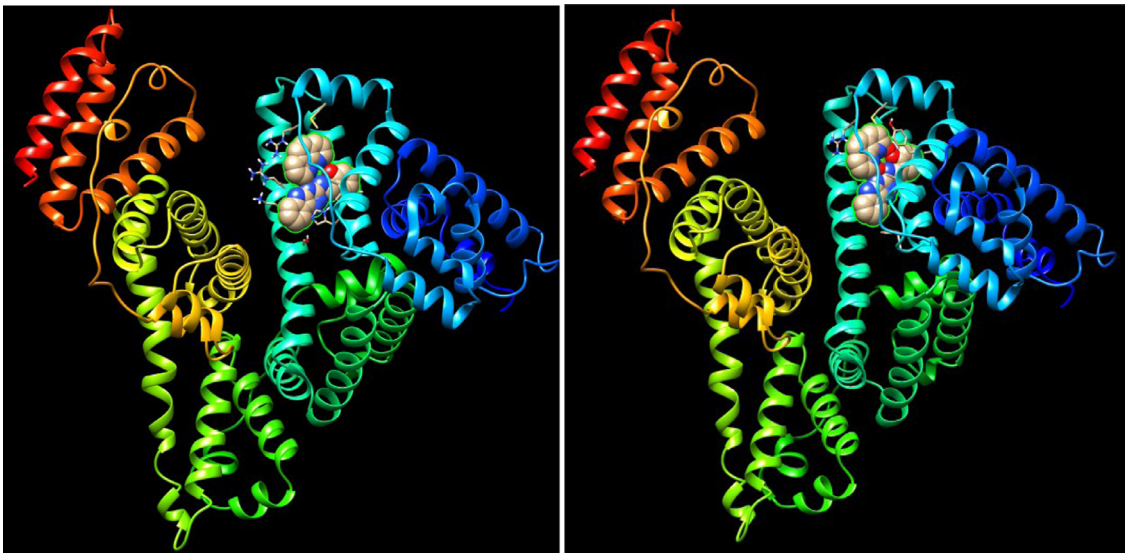

Fig. 9. Molecular docked poses of (a) complex **3** and (b) complex **4** lying in the hydrophobic cavity in subdomain IIA of HSA.

3.9. Molecular docking studies with HSA

Molecular docking studies of complexes **3** and **4** have been conducted to determine the exact binding location with HSA as it is considered as the main blood carrier protein (60%) for the transportation of the drugs and other endogenous substances. It is well established that HSA is a helicoidal protein and contains three homologous domains denoted as I, II and III. Each domain is further divided into two subdomains A and B which shared common helical motifs joined together by an extended polypeptide chain [99]. The binding sites for the drugs are located in the subdomain IIA and IIIA also known as the Sudlow site I and II, respectively. Apart from this, there is another site located in the subdomain IB which binds the heme, protoporphyrin IX and other synthetics porphyrins [100]. The docked conformation of complexes **3** and **4** with HSA protein revealed that both the complexes were exactly fitted into the hydrophobic cavity of site I located in the subdomain IIA. As depicted in Fig. 9, complex **4** was more embedded in the cavity

as compared to complex **3** indicating the stronger interaction of complex **4** with HSA. It is observed that both the molecules are closely located to Trp–214 residue which is also lying in the binding pocket of subdomain IIA. Besides the hydrophobic interaction, the complexes were also stabilized with the pocket by the hydrogen bonding interactions promoted by the phenolate oxygen and the nitrogen atoms of the triazine ring with the various amino acid groups. The binding affinity score in the optimum pose was found to be −7.02 and −7.34 kcal/mol for complexes **3** and **4**, respectively. Overall the molecular docking studies are consistent with the experimental studies and help us to get insight into the binding sites of metal complexes within the particular subdomain.

4. Conclusion

In this investigation, we have discussed the comparative DNA and HSA binding profile of the newly synthesized metal complexes [Ni(L)(Bipy)]1/2SO_4 (**1**), [Cu(L)(Bipy)]1/2SO_4 (**2**), [Ni(L)(Phen)]1/2SO_4 (**3**) and [Cu(L)(Phen)]1/2SO_4 (**4**) derived from new ligand (E)–2–(((5H–[1,2,4]triazino[5,6–b]indol–3–yl)imino)methyl)phenol (**L**) and 2,2′–Bipyridine/1,10 phenanthroline. The analysis of DNA binding of ligand **L** and metal complexes **1**–**4** from vivid biophysical techniques revealed that metal complexes **1**–**4** exhibited higher binding propensity than ligand (**L**) and prefer the electrostatic mode of interaction followed by partial intercalation. Complexes **3** and **4** containing the planar 1,10 phenanthroline ring displayed greater binding affinity as compared to **1** and **2** which contain bipyridine rings. Additionally, the HSA binding studies showed that complexes **3** and **4** interact efficiently with Trp–214 residues of HSA located in the subdomain IIA.

Declaration of Competing Interest

The authors declare that they have no known competing financial interests or personal relationships that could have appeared to influence the work reported in this paper.

CRediT authorship contribution statement

Reem L.B. Alanazi: Data curation, Investigation. **Mehvash Zaki:** Conceptualization, Methodology, Validation, Visualization, Formal analysis, Supervision, Writing – original draft, Writing – review & editing. **Wafa A. Bawazir:** Methodology, Resources, Project administration.

Acknowledgments

Dr. Mehvash Zaki and Wafa A. Bawazir acknowledges with thanks King Abdulaziz University and King Fahad Medical Research Center for technically supporting this work. The author Reem Alanazi is grateful to King Abdulaziz University and Hafr Al–Batin University for financial support. The authors are highly thankful to Dr. Mohd Afzal, King Saud University, Saudi Arabia for his valuable suggestions during the revision process of this manuscript.

Supplementary materials

Supplementary material associated with this article can be found, in the online version, at doi:10.1016/j.molstruc.2021.131203.

References

[1] A. Barve, A. Kumbhar, M. Bhat, B. Joshi, R. Butcher, U. Sonawane, R. Joshi, Mixed-ligand copper (II) maltolate complexes: synthesis, characterization, DNA binding and cleavage, and cytotoxicity, Inorg. Chem. 48 (2009) 9120–9132, doi:10.1021/ic9004642.

[2] P.C. Bruijnincx, P.J. Sadler, New trends for metal complexes with anticancer activity, Curr. Opin. Chem. Biol. 12 (2008) 197–206, doi:10.1016/j.cbpa.2007.11.013.

[3] K. Abdi, H. Hadadzadeh, M. Salimi, J. Simpson, A.D. Khalaji, A mononuclear copper (II) complex based on the polypyridyl ligand 2, 4, 6-tris (2-pyridyl)-1, 3, 5-triazine (tptz),[Cu (tptz)$_2$]$^{2+}$: X-ray crystal structure, DNA binding and *in vitro* cell cytotoxicity, Polyhedron 44 (2012) 101–112, doi:10.1016/j.poly.2012.06.089.

[4] K. Zhang, V. Wing–Wah Yam, Platinum (ii) non-covalent crosslinkers for supramolecular DNA hydrogels, Chem. Sci. 11 (2020) 3241–3249, doi:10.1039/C9SC05910E.

[5] A. Kellett, Z. Molphy, C. Slator, V. McKee, N.P. Farrell, Molecular methods for assessment of non-covalent metallodrug–DNA interactions, Chem. Soc. Rev. 48 (2019) 971–988, doi:10.1039/C8CS00157J.

[6] W. Xi, F.Q. Song, X.L. Xia, X.Q. Song, Tuned structure and DNA binding properties of metal complexes based on a new 4-acylpyrazolone derivative, New J. Chem. 44 (2020) 2281–2290, doi:10.1039/C9NJ05948B.

[7] M. Shoeb, R. Shaikh, Synthesis, spectral characterization and antibacterial activity of quinolone incorporating 1, 2, 4-triazine rings, Chem. Biol. Inter. 10 (2020) 51–55.

[8] S. Cascioferro, B. Parrino, V. Spano, A. Carbone, A. Montalbano, P. Barraja, P. Diana, G. Cirrincione, An overview on the recent developments of 1, 2, 4-triazine derivatives as anticancer compounds, Eur. J. Med. Chem. 142 (2017) 328–375, doi:10.1016/j.ejmech.2017.08.009.

[9] M.H. El–Wakil, A.F. El–Yazbi, H.M.A. Ashour, M.A. Khalil, K.A. Ismail, I.M. Labouta, Discovery of a novel DNA binding agent via design and synthesis of new thiazole hybrids and fused 1, 2, 4-triazines as potential antitumor agents: Computational, spectrometric and in silico studies, Bioorg. Chem. 90 (2019) 103089, doi:10.1016/j.bioorg.2019.103089.

[10] A. Lauria, A. Alfio, R. Bonsignore, C. Gentile, A. Martorana, G. Gennaro, G. Barone, A. Terenzi, A.M. Almerico, New benzothieno [3, 2-d]-1, 2, 3-triazines with antiproliferative activity: Synthesis, spectroscopic studies, and biological activity, Bioorg. Med. Chem. Lett. 24 (2014) 3291–3297, doi:10.1016/j.bmcl.2014.06.007.

[11] R.S. Ali, H.A. Saad, Synthesis of some novel fused pyrimido[4″,5″:5′,6′]-[1,2,4]triazino[3′,4′:3,4] [1,2,4]triazino[5,6-b]indoles with expected anticancer activity, Molecules 23 (2018) 693, doi:10.3390/molecules23030693.

[12] K. Ramesh, S.N. Murthy, K. Karnakar, Y.V.D. Nageswar, A facile, aqueous phase green synthetic protocol for the synthesis of 5,9b-dihydro-1*H*-[1,2,4]triazino[5,6-*b*]indole-3-ols/5,9b-dihydro-1*H*-[1,2,4]triazino[5,6-*b*]indole-3-thiols, Tetrahedron Lett. 52 (2011) 4734–4737, doi:10.1016/j.tetlet.2011.06.098.

[13] J.L. Kgokong, P.P. Smith, ad G.M. Matsabisa, 1,2,4-Triazino-[5,6b]indole derivatives: effects of the trifluoromethyl group on *in vitro* antimalarial activity, Bioorg. Med. Chem. 13 (2005) 2935–2942, doi:10.1016/j.bmc.2005.02.017.

[14] A. Keivanloo, S. Sepehri, M. Bakherad, M. Eskandari, Click Synthesis of 1,2,3-Triazoles-Linked 1,2,4-Triazino[5,6-b]indole, antibacterial activities and molecular docking studies, ChemistrySelect 5 (2020) 4091–4098, doi:10.1002/slct.202000266.

[15] A.G. Al Osaimi, R.S. Ali, H.A. Saada, M.R. El Sayed Aly, Synthesis and antimicrobial activity of novel fused [1, 2, 4]triazino[5, 6-b]indole derivatives, Russ. J. Gen. Chem. 87 (2017) 1246–1255, doi:10.1134/S1070363217060202.

[16] J.M.Z. Gladych, R. Hornby, J.H. Hunt, D. Jack, J.J. Boyle, R.J. Ferlauto, R.F. Haff, C.G. Kormendy, F.J. Stanfield, R.C. Stewart, Antiviral agents. 5H-as-Triazino[5,6-b]indoles, J. Med. Chem. 15 (1972) 277–281, doi:10.1021/jm00273a017.

[17] L. Pathaw, T. Khamrang, A. Kathiravan, M. Velusamy, Synthesis, crystal structure, bovine serum albumin binding studies of 1, 2, 4-triazine based copper (I) complexes, J. Mol. Struc. 1207 (2020) 127821, doi:10.1016/j.molstruc.2020.127821.

[18] E. Bulatov, R. Sayarova, R. Mingaleeva, R. Miftakhova, M. Gomzikova, Y. Ignatyev, A. Petukhov, P. Davidovich, A. Rizvanov, N.A. Barlev, Isatin-Schiff base-copper (II) complex induces cell death in p53-positive tumors, Cell Death Discov. 4 (2018) 103, doi:10.1038/s41420-018-0120-z.

[19] M. Lashanizadegan, H.A. Ashari, M. Sarkheil, M. Anafcheh, S. Jahangiry, New Cu (II), Co (II) and Ni (II) azo-Schiff base complexes: synthesis, characterization, catalytic oxidation of alkenes and DFT study, Polyhedron 200 (2021) 115148, doi:10.1016/j.poly.2021.115148.

[20] H. Kargar, A.A. Ardakani, M.N. Tahir, M. Ashfaq, K.S. Munawar, Synthesis, spectral characterization, crystal structure determination and antimicrobial activity of Ni (II), Cu (II) and Zn (II) complexes with the Schiff base ligand derived from 3, 5-dibromosalicylaldehyde, J. Mol. Struct. 1229 (2021) 129842, doi:10.1016/j.molstruc.2020.129842.

[21] N. Amir, Y. Miyashita, K. Fujisawa, K.-I. Okamoto, Nickel (II) complexes with Schiff bases derived from salicylaldehyde or pentanedione and 3-aminopropanethiol, J. Coord. Chem. 59 (2006) 1527–1536, doi:10.1080/00958970500537796.

[22] O.A. Chaves, L.B. Menezes, B.A. Iglesias, Multiple spectroscopic and theoretical investigation of meso-tetra-(4-pyridyl) porphyrinruthenium (II) complexes in HSA-binding studies. Effect of Zn (II) in protein binding, J. Mol. Liq. 294 (2019) 111581, doi:10.1016/j.molliq.2019.111581.

[23] C. Zhu, F. Liu, Y. Wei, F. Zhang, T. Pan, Y. Ye, Y. Shen, Evaluating the potential risk by probing the site-selective binding of rutin-Pr (III) complex to human serum albumin, Food Chem. Toxicol. 148 (2021) 111927, doi:10.1016/j.fct.2020.111927.

[24] F. Shen, Y.–X. Liu, S.–M. Li, C.–K. Jiang, B.–F. Wang, Y.–H. Xiong, Z.–W. Mao, X.–Y. Le, Synthesis, crystal structures, molecular docking and *in vitro* cy-

totoxicity studies of two new copper (ii) complexes: special emphasis on their binding to HSA, New J. Chem. 41 (2017) 12429–12441, doi:10.1039/C7NJ02351K.
[25] H. Shi, T. Fang, Y. Tian, H. Huang, Y. Liu, A dual-fluorescent nano-carrier for delivering photoactive ruthenium polypyridyl complexes, J. Mater. Chem. B 4 (2016) 4746–4753, doi:10.1039/C6TB01070A.
[26] A. Wolfe, G.H. Shimer, T. Meehan, Polycyclic aromatic hydrocarbons physically intercalate into duplex regions of denatured DNA, Biochemistry 26 (1987) 6392–6396, doi:10.1021/bi00394a013.
[27] H.G. Weder, J. Schildknecet, R.A. Lutz, P. Kesselrinu, Determination of binding parameters from Scatchard plots: theoretical and practical considerations, Eur. J. Biochem. 42 (1974) 475–481, doi:10.1111/j.1432-1033.1974.tb03361.x.
[28] C. Tan, J. Liu, W.Zheng H.Li, S. Shi, L. Chen, L. Ji, Differences in structure, physiological stability, electrochemistry, cytotoxicity, DNA and protein binding properties between two Ru (III) complexes, J. Inorg. Biochem 102 (2008) 347–358, doi:10.1016/j.jinorgbio.2007.09.008.
[29] D. Mustard, D.W. Ritchie, Docking essential dynamics eigenstructures, Proteins Struct. Funct. Bioinform. 60 (2005) 269–274, doi:10.1002/prot.20569.
[30] N. Ganji, S. Daravath, A. Rambabu, K. Venkateswarlu, D.S. Shankar, Shivaraj, Exploration of DNA interaction, antimicrobial and antioxidant studies on binary transition metal complexes with isoxazole Schiff bases: Preparation and spectral characterization, Inorg. Chem. Commun. 121 (2020) 108247, doi:10.1016/j.inoche.2020.108247.
[31] S.–Z. Zhang, G. Guo, W.–M. Ding, J. Li, Y. Wu, H.–J. Zhang, J.–Q. Guo, Y.–X. Sun, Synthesis and spectroscopic properties of two different structural Schiff base Zn (II) complexes constructed with/without auxiliary ligands, J. Mol. Struct. 1230 (2021) 129627, doi:10.1016/j.molstruc.2020.129627.
[32] B. Vivekanand, K.M. Raj, B.H.M. Mruthyunjayaswamy, Synthesis, characterization, antimicrobial, DNA-cleavage and antioxidant activities of 3-((5-chloro-2-phenyl-1H-indol-3-ylimino) methyl) quinoline-2 (1H)-thione and its metal complexes, J. Mol. Struct. 1079 (2015) 214–224, doi:10.1016/j.molstruc.2014.08.033.
[33] K.M. Raj, B.H.M. Mruthyunjayaswamy, Synthesis, spectroscopic characterization, electrochemistry and biological activity evaluation of some metal (II) complexes with ONO donor ligands containing indole and coumarin moieties, J. Saudi Chem. Soc. 21 (2017) S202–S218, doi:10.1016/j.jscs.2014.01.001.
[34] H. Arslan, A. Demircan, Structure and Vibrational Spectra of Tert-butyl N-(2-bromocyclohex-2-enyl)-N-(2-furylmethyl)carbamate, Acta Phys. Chim. Sinica 23 (2007) 1683–1690 10.1016/S1872-1508(07)60082-5.
[35] B.C. Smith, IR spectral interpretation workshop alcohols the rest of the story, Spectroscopy 32 (2017) 19–23 https://www.spectroscopyonline.com/view/alcohols-rest-story-alf3.
[36] R. Fouad, O.M.I. Adly, Novel Cu^{2+} and Zn^{2+} nanocomplexes drug based on hydrazone ligand bearings chromone and triazine moieties: Structural, spectral, DFT, molecular docking and cytotoxic studies, J. Mol. Struct. 1225 (2021) 129158, doi:10.1016/j.molstruc.2020.129158.
[37] O.A. EL–Gammal, H. Alshater, H.A. El–Boraey, Schiff base metal complexes of 4-methyl-1H-indol-3-carbaldehyde derivative as a series of potential antioxidants and antimicrobial: Synthesis, spectroscopic characterization and 3D molecular modeling, J. Mol. Struct. 1195 (2019) 220–230, doi:10.1016/j.molstruc.2019.05.101.
[38] S. Alyar, U.O. Ozmen, S. Adem, H. Alyar, E. Bilen, K. Kaya, Synthesis, spectroscopic characterizations, carbonic anhydrase II inhibitory activity, anticancer activity and docking studies of new Schiff bases of sulfa drugs, J. Mol. Struct. 1223 (2021) 128911, doi:10.1016/j.molstruc.2020.128911.
[39] M.H. Abdelrahman, A.S. Aboraia, B.G.M. Youssif, B.E.M. Elsadek, Design, synthesis and pharmacophoric model building of new 3-alkoxymethyl/3-phenyl indole-2-carboxamides with potential antiproliferative activity, Chem. Biol. Drug Des. 90 (2017) 64–82, doi:10.1111/cbdd.12928.
[40] Y. Sun, Y. Liu, W. Guo, Fluorescent and chromogenic probes bearing salicylaldehyde hydrazone functionality for cyanide detection in aqueous solution, Sens. Actuators B Chem. 143 (2009) 171–176, doi:10.1016/j.snb.2009.09.038.
[41] Z.H.A. El–Wahab, Mononuclear metal complexes of organic carboxylic acid derivatives: Synthesis, spectroscopic characterization, thermal investigation and antimicrobial activity, Spectrochim. Acta A 67 (2007) 25–38, doi:10.1016/j.saa.2006.05.038.
[42] Y. Xu, T. Watermann, H.–H. Limbach, T. Gutmann, D. Sebastiani, G. Buntkowsky, Water and small organic molecules as probes for geometric confinement in well-ordered mesoporous carbon materials, Phys. Chem. Chem. Phys. 16 (2014) 9327–9336, doi:10.1039/C4CP00808A.
[43] H.E. Gottlieb, V. Kotlyar, A. Nudelman, NMR chemical shifts of common laboratory solvents as trace impurities, J. Org. Chem. 62 (1997) 7512–7515, doi:10.1021/jo971176v.
[44] M.S. Almutairi, S. Xavier, M. Sathish, H.A. Ghabbour, S. Sebastian, S. Periandy, Reem I. Al–Wabli, Mohamed I. Attia, Spectroscopic (FT-IR, FT-Raman, UV, 1H and 13C NMR) profiling and computational studies on methyl 5-methoxy-1H-indole-2-carboxylate: A potential precursor to biologically active molecules, J. Mol. Struct. 1133 (2017) 199–210, doi:10.1016/j.molstruc.2016.12.004.
[45] M. Yildiz, O. Karpuz, C.T. Zeyrek, B. Boyacioglu, H. Dal, N. Demir, N. Yildirim, H. Unver, Synthesis, biological activity, DNA binding and anion sensors, molecular structure and quantum chemical studies of a novel bidentate Schiff base derived from 3, 5-bis (triflouromethyl) aniline and salicylaldehyde, J. Mol. Struct. 1094 (2015) 148–160, doi:10.1016/j.molstruc.2015.03.047.
[46] D.M. Boghaei, M. Gharagozlou, Spectral characterization of novel ternary zinc (II) complexes containing 1, 10-phenanthroline and Schiff bases derived from amino acids and salicylaldehyde-5-sulfonates, Spectrochim. Acta A 67 (2007) 944–949, doi:10.1016/j.saa.2006.09.012.
[47] L.F. Hernandez–Ayala, M. Flores–Alamo, S. Escalante–Tovar, R. Galindo–Murillo, J.C. Garcia–Ramos, J. Garcia–Valdes, V. Gomez–Vidales, K. Resendiz–Acevedo, Y. Toledano–Magana, L. Ruiz–Azuara, Synthesis, characterization, theoretical studies and biological activity of coordination compounds with essential metals containing N4-donor ligand 2, 9-di (ethylaminomethyl)-1, 10-phenanthroline, Inorg. Chim. Acta 470 (2018) 187–196, doi:10.1016/j.ica.2017.06.040.
[48] R. Kalarani, M. Sankarganesh, G.G. Vinoth Kumar, M. Kalanithi, Synthesis, spectral, DFT calculation, sensor, antimicrobial and DNA binding studies of Co (II), Cu (II) and Zn (II) metal complexes with 2-amino benzimidazole Schiff base, J. Mol. Struct. 1206 (2020) 127725, doi:10.1016/j.molstruc.2020.127725.
[49] I. Nawrot, B. Machura, R. Kruszynski, Thiocyanate cadmium (II) complexes of 2, 4, 6-tri (2-pyridyl)-1, 3, 5-triazine–Synthesis, structure and luminescence properties, J. Lumin. 156 (2014) 240–254, doi:10.1016/j.jlumin.2014.08.022.
[50] C.E. Satheesh, P. Raghavendra Kumar, P.A. Suchetan, H. Rajanaika, S Foro, New (N, O) Schiff bases of 2-hydroxynaphthaldehyde and their homoleptic Zn (II) and Cu (II) complexes–Synthesis, structural characterization, Hirshfeld surface analysis and antimicrobial activity studies, Inorg. Chim. Acta 515 (2021) 120017, doi:10.1016/j.ica.2020.120017.
[51] A.M. Mansour, O.R. Shehab, Spectroscopic and TDDFT studies of N-phenyl-N′-(3-triazolyl) thiourea) compounds with transition metal ions, Arab. J. Chem. 14 (2021) 102932, doi:10.1016/j.arabjc.2020.102932.
[52] T.A. Fayed, M. Gaber, M.N. El–Nahass, H.A. Diab, M.M. El–Gamil, Synthesis, Structural characterization, thermal, molecular modeling and biological studies of chalcone and Cr (III), Mn (II), Cu (II) Zn (II) and Cd (II) chelates, J. Mol. Struct. 1221 (2020) 128742, doi:10.1016/j.molstruc.2020.128742.
[53] A. Gusev, V. Shulgin, E. Braga, E. Zamnius, M. Kryukova, W. Linert, Luminescent properties of Zn complexes based on tetradentate N2O2-donor pyrazolone schiff bases, Dyes Pigm 183 (2020) 108626, doi:10.1016/j.dyepig.2020.108626.
[54] H. Farrokhpour, H. Hadadzadeh, F. Darabi, F. Abyar, H.A. Rudbari, T. Ahmadi–Bagheri, A rare dihydroxo copper (II) complex with ciprofloxacin; a combined experimental and ONIOM computational study of the interaction of the complex with DNA and BSA, RSC Adv. 4 (2014) 35390–35404, doi:10.1039/C4RA04634J.
[55] E.S. Aazam, M. Zaki, Synthesis and Characterization of Ni (II)/Zn (II) Metal complexes derived from Schiff base and Ortho-phenylenediamine: *In vitro* DNA binding, molecular modeling and RBC hemolysis, ChemistrySelect 5 (2020) 610–618, doi:10.1002/slct.201903583.
[56] P. Alreja, N. Kaur, DNA and copper (II) governed fluorescence tuning of phenanthroline possessing Ru (II) complex. Interplay of electrostatic interactions, Inorg. Chem. Commun. 77 (2017) 51–54, doi:10.1016/j.inoche.2017.01.033.
[57] B. Kaya, Z.K. Yilmaz, O. Sahin, B. Aslim, B. Ulkuseven, Structural characterization of new zinc (ii) complexes with N 2 O 2 chelating thiosemicarbazidato ligands; investigation of the relationship between their DNA interaction and *in vitro* antiproliferative activity towards human cancer cells, New J. Chem. 44 (2020) 9313–9320 10.1039/D0NJ02149K.
[58] B.K. Kundu, S.M.Mobin Pragti, S. Mukhopadhyay, Studies on the influence of the nuclearity of zinc (ii) hemi-salen complexes on some pivotal biological applications, Dalton Trans. 49 (2020) 15481–15503, doi:10.1039/D0DT02941F.
[59] H. Irving, R.J.P. Williams, The stability of transition-metal complexes, J. Chem. Soc. 637 (1953) 3192–3210, doi:10.1039/JR9530003192.
[60] R. Loganathan, S. Ramakrishnan, M. Ganeshpandian, N.S. Bhuvanesh, M. Palaniandavar, A. Riyasdeen, M.A. Akbarsha, Mixed ligand copper(ii) dicarboxylate complexes: the role of co-ligand hydrophobicity in DNA binding, double-strand DNA cleavage, protein binding and cytotoxicity, Dalton Trans. 44 (2015) 10210–10227, doi:10.1039/C4DT03879G.
[61] R. Patel, N. Singh, K. Shukla, J. Niclos-Gutierrez, A. Castineiras, V. Vaidyanathan, B.U. Nair, Characterization and biological activities of two copper(II) complexes with diethylenetriamine and 2,2′-bipyridine or 1,10-phenanthroline as ligands, Spectrochim. Acta, Part A 62 (2005) 261–268, doi:10.1016/j.saa.2004.12.034.
[62] I. Turel, The interactions of metal ions with quinolone antibacterial agents, Coord. Chem. Rev. 232 (2002) 27–47, doi:10.1016/S0010-8545(02)00027-9.
[63] M. Sharma, M. Ganeshpandian, M. Majumder, A. Tamilarasan, M. Sharma, R. Mukhopadhyay, N.S. Islam, M. Palaniandavar, Octahedral copper (ii)-diimine complexes of triethylenetetramine: effect of stereochemical fluxionality and ligand hydrophobicity on Cu II/Cu I redox, DNA binding and cleavage, cytotoxicity and apoptosis-inducing ability, Dalton Trans. 49 (2020) 8282–8297, doi:10.1039/D0DT00928H.
[64] T.H. Sanatkar, H. Hadadzadeh, Z. Jannesari, T. Khayamian, M. Ebrahimi, H.A. Rudbari, M. Torkzadeh-Mahani, M. Anjomshoa, Characterization, photocleavage, molecular modeling, and DNA-and BSA-binding studies of Cu (II) and Ni (II) complexes with the non-steroidal anti-inflammatory drug meloxicam, Inorg. Chim. Acta 423 (2014) 256–272, doi:10.1016/j.ica.2014.08.060.
[65] A.A. Ensafi, R. Hajiana, S. Ebrahimi, Study on the interaction between morin-Bi (III) complex and DNA with the use of methylene blue dye as a fluorophor probe, J. Braz. Chem. Soc. 20 (2009) 266–276, doi:10.1590/S0103-50532009000200011.
[66] V.G. Vaidyanathan, B.U. Nair, Synthesis, characterization, and DNA binding studies of a chromium (III) complex containing a tridentate ligand, Eur. J. Inorg. Chem. (2003) 3633–3638, doi:10.1002/ejic.200300170.

[67] N. Shahabadi, S. Mohammadi, R. Alizadeh, Bioinorg. DNA interaction studies of a new platinum(II) complex containing different aromatic Dinitrogen ligands, Chem. Appl. (2011) 429241, doi:10.1155/2011/429241.
[68] H. Liu, C. Hao, Z. Nan, H. Qu, X. Zhang, Z. Zhang, R. Sun, Fabrication of graphene oxide and sliver nanoparticle hybrids for fluorescence quenching of DNA labeled by methylene blue, Spectrochim. Acta A 243 (2020) 118802, doi:10.1016/j.saa.2020.118802.
[69] A. Petrovic, M. Zivanovic, R. Puchta, D. Cocic, A. Scheurer, N. Milivojevic, J. Bogojeski, Experimental and quantum chemical study on the DNA/protein binding and the biological activity of a rhodium (III) complex with 1, 2, 4-triazole as an inert ligand, Dalton Trans 49 (2020) 9070–9085, doi:10.1039/D0DT01343A.
[70] N. Ganji, S. Daravath, A. Rambabu, K. Venkateswarlu, D.S. Shankar, Shivaraj, Exploration of DNA interaction, antimicrobial and antioxidant studies on binary transition metal complexes with isoxazole Schiff bases: Preparation and spectral characterization, Inorg. Chem. Commun. 121 (2020) 108247, doi:10.1016/j.inoche.2020.108247.
[71] N.N. Rao, E. Kishan, K. Gopichand, R. Nagaraju, A.M. Ganai, P.V. Rao, Design, synthesis, spectral characterization, DNA binding, photo cleavage and antibacterial studies of transition metal complexes of benzothiazole Schiff base, Chem. Data Collec. 27 (2020) 100368, doi:10.1016/j.cdc.2020.100368.
[72] R.R. Kumar, M.K.M. Subarkhan, R. Ramesh, Synthesis and structure of nickel (II) thiocarboxamide complexes: effect of ligand substitutions on DNA/protein binding, antioxidant and cytotoxicity, Rsc Adv. 5 (2015) 46760–46773, doi:10.1039/C5RA06112A.
[73] P. Adak, B. Ghosh, A. Bauza, A. Frontera, S.R. Herronc, S.K. Chattopadhyay, Binuclear and tetranuclear Zn (II) complexes with thiosemicarbazones: synthesis, X-ray crystal structures, ATP-sensing, DNA-binding, phosphatase activity and theoretical calculations, Rsc Adv. 10 (2020) 12735–12746, doi:10.1039/C9RA10549B.
[74] V.A. Kawade, A.A. Kumbhar, A.S. Kumbhar, C. Nather, A. Erxleben, U.B. Sonawane, R.R. Joshi, Mixed ligand cobalt (II) picolinate complexes: synthesis, characterization, DNA binding and photocleavage, Dalton Trans. 40 (2011) 639–650, doi:10.1039/C0DT01078B.
[75] G. Devagi, F. Reyhaneh, F. Dallemer, R. Jayakumar, P. Kalaivani, R. Prabhakaran, Morphological and *in vitro* evaluation of programmed cell death in MCF-7 cells by new organoruthenium (II) complexes, New J. Chem. 41 (2017) 8620–8636, doi:10.1039/C7NJ01707C.
[76] F. Shen, Y.–X. Liu, S.–M. Li, C.–K. Jiang, B.–F. Wang, Y.–H. Xiong, Z.–W. Mao, X.–Y. Le, Synthesis, crystal structures, molecular docking and *in vitro* cytotoxicity studies of two new copper (ii) complexes: special emphasis on their binding to HSA, New J. Chem. 41 (2017) 12429–12441, doi:10.1039/C7NJ02351K.
[77] K. Karami, N. Jamshidian, A. Bagheri, A. Hajiaghasi, A.A. Momtazi–Borojeni, E. Abdollahi, A. Shahpiri, N. Azizi, J. Lipkowski, Novel fluorescence palladium-alkoxime complexes: Synthesis, characterization, DNA/BSA spectroscopic and docking studies, evaluation of cytotoxicity and DNA cleavage mechanism, J. Mol. Struct. 1206 (2020) 127595, doi:10.1016/j.molstruc.2019.127595.
[78] M.B. Dukic, M.S. Jeremic, I.P. Filipovic, O.R. Klisuric, V.V. Kojic, D.S. Jakimov, R.M. Jelic, V. Onnis, Z.D. Matovic, Synthesis, characterization, HSA/DNA interactions and antitumor activity of new [Ru (η^6-p-cymene)Cl_2(L)] complexes, J. Inorg. Biochem. 213 (2020) 111256, doi:10.1016/j.jinorgbio.2020.111256.
[79] X.–Bing. Fu, G.–Tian. Weng, D.–D. Liu, X.–Y. Le, Synthesis, characterization, DNA binding and cleavage, HSA interaction and cytotoxicity of a new copper(II) complex derived from 2-(2′-pyridyl)benzothiazole and glycylglycine, J. Photochem. Photobiol. A 276 (2014) 83–95, doi:10.1016/j.jphotochem.2013.12.002.
[80] S.U. Parsekar, P. Velankanni, S. Sridhar, P. Haldar, N.A. Mate, A. Banerjee, P.K.S. Antharjanam, A.P. Koley, M. Kumar, Protein binding studies with human serum albumin, molecular docking and *in vitro* cytotoxicity studies using HeLa cervical carcinoma cells of Cu (II)/Zn (II) complexes containing a carbohydrazone ligand, Dalton Trans. 49 (2020) 2947–2965, doi:10.1039/C9DT04656A.
[81] S. Al-Harthi, J.I. Lachowicz, M.E. Nowakowski, M. Jaremko, L. Jaremko, Towards the functional high-resolution coordination chemistry of blood plasma human serum albumin, J. Inorg. Biochem. 198 (2019) 110716, doi:10.1016/j.jinorgbio.2019.110716.
[82] M. Sendzik, M.J. Pushie, Ew. Stefaniak, K.L. Haas, Structure and Affinity of Cu(I) bound to human serum albumin, Inorg. Chem. 56 (2017) 15057–15065 DOI: 10.1021/acs.inorgchem.7b02397.
[83] V.K.A. Kalalbandi, J. Seetharamappa, 1-[(2 E)-3-Phenylprop-2-enoyl]-1 H-benzimidazoles as anticancer agents: synthesis, crystal structure analysis and binding studies of the most potent anticancer molecule with serum albumin, Med. Chem. Commun. 6 (2015) 1942–1953, doi:10.1039/C5MD00293A.
[84] N. Chadha, D. Singh, M.D. Milton, G. Mishra, J. Danield, A.K. Mishra, A.K. Tiwari, Computational prediction of interaction and pharmacokinetics profile study for polyamino-polycarboxylic ligands on binding with human serum albumin, New J. Chem. 44 (2020) 2907–2918, doi:10.1039/C9NJ05594K.
[85] C.–L. Zhang, Y.–X. Liu, X.–M. Zhang, S. Chen, F. Shen, Y.–H. Xiong, W. Liu, Z.–W. Mao, X.–Y. Le, Synthesis, characterization, DNA/HSA interactions and *in vitro* cytotoxic activities of two novel water-soluble copper (II) complexes with 1, 3, 5-triazine derivative ligand and amino acids, Mater. Sci. Engineer. C 91 (2018) 414–425, doi:10.1016/j.msec.2018.05.065.
[86] O.A. Chaves, L.B. Menezes, B.A. Iglesias, Multiple spectroscopic and theoretical investigation of meso-tetra-(4-pyridyl) porphyrinruthenium (II) complexes in HSA-binding studies. Effect of Zn (II) in protein binding, J. Mol. Liq. 294 (2019) 111581, doi:10.1016/j.molliq.2019.111581.
[87] A. Bhattacharjee, S. Das, B. Das, P. Roy, Intercalative DNA binding, protein binding, antibacterial activities and cytotoxicity studies of a mononuclear copper (II) complex, Inorg. Chim. Acta 514 (2021) 119961, doi:10.1016/j.ica.2020.119961.
[88] F.F. Tian, J.H. Li, F.L. Jiang, X.L. Han, C. Xiang, Y.S. Ge, L.L. Li, Y. Liu, Investigating the interactions of a novel anticancer delocalized lipophilic cation and its precursor compound with human serum albumin, RSC Adv. 2 (2012) 501–513, doi:10.1039/C1RA00521A.
[89] D. Yinhua, M.M. Foroughi, Z. Aramesh–Boroujeni, d S. Jahani, M. Peydayesh, F. Borhani, M. Khatami, M. Rohani, M. Dusek, V. Eigner, The synthesis, characterization, DNA/BSA/HSA interactions, molecular modeling, antibacterial properties, and *in vitro* cytotoxic activities of novel parent and niosome nano-encapsulated Ho (III) complexes, RSC Adv. 10 (2020) 22891–22908, doi:10.1039/D0RA03436C.
[90] O.H. Laitinen, V.P. Hytonen, H.R. Nordlund, M.S. Kuloma, Genetically engineered avidins and streptavidins, Cell. Mol. Life Sci. 63 (2006) 29920–23017, doi:10.1007/s00018-006-6288-z.
[91] T. Peters, F.A. Blumenstock, Copper-binding properties of bovine serum albumin and its amino-terminal peptide fragment, J. Biol. Chem. 242 (1967) 1574–1578, doi:10.1016/S0021-9258(18)96130-2.
[92] T. Kirsipuu, A. Zadoroznaja, J. Smirnova, M. Friedemann, T. Plitz, V. Tougu, P. Palumaa, Copper(II)-binding equilibria in human blood, Scientific Rep. 10 (2020) 5686, doi:10.1038/s41598-020-62560-4.
[93] H. Kabeer, S. Hanif, A. Arsalan, S. Asmat, H. Younus, M. Shakir, Structural-dependent N, O-donor imine-appended Cu(II)/Zn(II) complexes: synthesis, spectral, and *in vitro* pharmacological assessment, ACS Omega 5 (2020) 1229–1245, doi:10.1021/acsomega.9b03762.
[94] S. Bhunia, S. Adhikary, P. Purkayastha, Energy transfer from luminescent gold nanoclusters to non-luminescent silver nanoparticles from a new perspective, J. Mol. Liq. 318 (2020) 114048, doi:10.1016/j.molliq.2020.114048.
[95] M. Dehkhodaei, M. Khorshidifard, H.A. Rudbari, M. Sahihi, G. Azimi, N. Habibi, S. Taheri, G. Bruno, R. Azadbakht, Synthesis, characterization, crystal structure and DNA, HSA-binding studies of four Schiff base complexes derived from salicylaldehyde and isopropylamine, Inorg. Chim. Acta 466 (2017) 48–60, doi:10.1016/j.ica.2017.05.035.
[96] P. Kumar, R.J. Butcher, A.K. Patra, Ternary Co (II), Ni (II) and Cu (II) complexes containing dipyridophenazine and saccharin: Structures, reactivity, binding interactions with biomolecules and DNA damage activity, Inorg. Chim. Acta 506 (2020) 119532, doi:10.1016/j.ica.2020.119532.
[97] R. Rohs, I. Bloch, H. Sklenar, Z. Shakked, Molecular flexibility in ab initio drug docking to DNA: binding-site and binding-mode transitions in all-atom Monte Carlo simulations, Nucl. Acids Res. 33 (2005) 7048–7057 10.1093/nar/gki1008.
[98] A. Jayamania, N. Sengottuvelan, G. Chakkaravarthi, Synthesis, structural, electrochemical, DNA interaction, antimicrobial and molecular docking studies on dimeric copper (II) complexes involving some potential bidentate ligands, Polyhedron 81 (2014) 764–776, doi:10.1016/j.poly.2014.05.076.
[99] S. Curry, H. Mandelkow, P. Brick, N. Franks, Crystal structure of human serum albumin complexed with fatty acid reveals an asymmetric distribution of binding sites, Nature Struct. Biol. 5 (1998) 827–835, doi:10.1038/1869.
[100] T.R.C. Guizado, Analysis of the structure and dynamics of human serum albumin, J. Mol. Model 20 (2014) 2450, doi:10.1007/s00894-014-2450-y.